34th Symposium on Naval Hydrodynamics
Washington, United States, 26th June - 01 July 2022

Numerical investigation of the JBC hull and propeller interaction under static drift condition

P. Sumislawski, A. Sahab, I. Shevchuk, M. Abdel-Maksoud
Institute for Fluid Dynamics and Ship Theory, Hamburg University of Technology (TUHH), Germany

ABSTRACT

As outlined in the Tokyo CFD Workshop 2015, reliably reproducing the turbulent kinetic energy and vorticity in the wake of the Japan Bulk Carrier (JBC) hull is still a challenge to contemporary CFD methods (Hino, et al., 2021). Depending on the applied turbulence modeling approach, a wide variance of fluid characteristics can be observed. In numerical simulations, the accuracy of resolving the stationary vortices induced along the ship hull and quantifying their strength is part of current research investigations (see Visonneau, et al., 2016, Shevchuk, et al., 2016). This topic is especially important for the static drift condition, under which the vortical structures can have a significant influence on the interaction between the hull and propeller and lead to high fluctuations of propeller and hull drift forces. The objective of this study is the numerical investigation of the hull-propeller interaction of the JBC hull under static drift condition. Taking the propeller into account leads to two different scenarios that are investigated: positive and negative drift. This results in two operational conditions of the propeller. Within the numerical study a RANS approach as well as DES methods are applied in order to investigate the influence of the applied turbulence model on the flow structure. The numerical model is validated based on extensive results from the Tomographic Particle Image Velocimetry measurements with and without propeller, which are presented and compared to the CFD results. A detailed analysis of hull and propeller forces will be presented in this paper.

INTRODUCTION

Due to the highly unsteady flow characteristics modeling of turbulent flows around ship hulls with high block coefficients has received a lot of attention in naval hydrodynamics over the past years. The steady development of hybrid turbulence models has laid important foundations for a reliable prediction of fluctuating flow characteristics. On the one hand, the prediction of the wake of a ship is a great challenge and, on the other hand, this very complex wake has a direct influence on the operating condition of the propeller. This connection becomes all the more important when, due to a static drift, the flow tends to become highly complicated compared to straight-ahead condition. The turbulent flow around a hull with high block coefficient is dominated by large separation areas and unsteady behavior. Many researchers address the challenge of predicting these flows mainly focusing on hull forms of the JBC bulk carrier (Visonneau, et al., 2016) and KVLCC2 (Ismail, et al., 2009, Xing, et al., 2012, Fureby, et al., 2016 and Feder, et al., 2019). The propeller thrust force has been investigated using hybrid methods under straight-ahead condition by Abbas, et al., 2015. The JBC hull has been investigated in detail under straight-ahead condition in the CFD workshop 2015 in detail (see Hino, et al., 2021). Here, many institutions contributed with CFD simulations based on RANS, LES or hybrid modeling approaches and came to the unified conclusion that hybrid modeling approaches are best able to predict TKE accurately. Since then, the researchers at Hamburg University of Technology (TUHH) have been focusing on the experimental and numerical investigation of the JBC test case. The close cooperation between CFD and EFD enabled major progress to be made.

Extensive measurements of the velocity field under static drift condition were carried out as a part of the PSDMan research project funded by the German Federal Ministry for Economic Affairs and Climate Action. The measurements with propellers are also a part of this project. The basic idea is to analyze the action of the propeller under different inflow conditions. The wind tunnel tests of the JBC hull at TUHH have been conducted at straight ahead and static drift conditions. The recently commissioned tomographic Particle Image Velocimetry (T-PIV) system is capable of measuring all three components of velocity with high temporal and spatial accuracy and therefore obtaining all components of vorticity and analyze the turbulent fluctuations in all three spatial directions, which is new compared to previously available stereoscopic PIV measurements. It provides

comprehensive measurement data for validation of the CFD simulations.

The JBC hull is a common benchmark for studies of turbulent flows around ship hulls and was introduced as a validation test case for the CFD workshop in 2015 by National Maritime Research Institute (NMRI). The ship is equipped with a right-handed 5-bladed screw propeller which is a part of the NMRI design (see Figure 1 and Table 2). The principle dimensions of the JBC hull are given in Table 1. Basically, the flow around the JBC hull at static drift contains two dominant vortical structures. First, the oblique flow in the bow region of the hull causes detachment close to the front shoulder and a formation of a vortex, see Figure 2. This vortex gains energy due to continuous detachment downstream. This vortex is referred to as FSV throughout the paper. In the rear area of the ship, another large-scale detachment occurs, which extends over the entire rear shoulder. This vortex is stronger than FSV and is called after body vortex (ABV). The choice of the measurement planes was made on the basis of the CFD results.

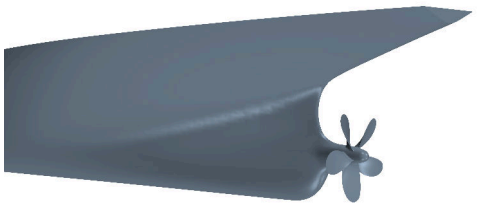

Figure 1: Aft region of JBC hull

Table 1: Hull main parameters

Ship length L_{pp} [m]	280.0
Breadth B [m]	45.2
Draft T [m]	16.6
Block coefficient c_B [–]	0.848
Model Scale λ [–]	79.7
Velocity u_∞ [m/s]	10
Drift angle β [deg]	8

The paper focuses on the numerical analysis of the propeller-hull interaction at static drift motion of the JBC hull at 8° using the commercial CFD code StarCCM+® (Version 14.06) by Siemens PLM. Assuming an upward z-axis, a positive drift angle means that the hull is turned to port. First, the bare hull of JBC is investigated under static drift condition using different turbulence modeling approaches, and then the results are validated with

Table 2: Propeller main parameters

Propeller diameter D_P [m]	0.102
Number blades [–]	5
Number pitch ratio [–]	0.75
Expanded area ratio [–]	0.5
Propeller rps n_p [1/s]	125
Propeller advance ratio J [–]	0.26

experimentally obtained data. For this purpose, flow measurements were carried out in the wind tunnel of TUHH, in which the flow and statistical fluctuations were determined in certain planes. Part of the investigation is the validation of the calculations for FSV and ABV. In the next step, drift calculations with propeller are presented. In each case, a distinction is made between positive and negative drift, since different flow conditions are observed under both circumstances. The calculations are performed with a constant propeller rotation rate. The inflow conditions of the propeller differ considerably in various test cases due to the different inflow angles. Based on these results, the hull forces and propeller blade forces for different radial sections are investigated. For comparison, selected simulations are compared to the straight-ahead condition. In addition, the propulsion of the arrangements is investigated. It should be mentioned that it was required to limit the number of revolutions of the propeller. This was necessary to reduce the Mach number and thus avoid compressibility. Moreover, high numbers of revolutions are associated with severe centrifugal forces which significantly increase the mechanical load on the model's structure. Therefore, the operating point of the propeller does not correspond to the propulsion point. This means that the propeller thrust achieved is significantly lower than the ship's resistance.

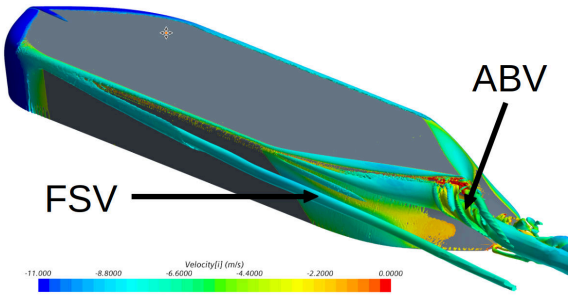

Figure 2: Vortex system of JBC hull at static drift

EXPERIMENTAL INVESTIGATION

The applied experimental data for validation of CFD calculations has been measured in the wind tunnel operated by the Institute for Fluid Dynamics and Ship Theory (FDS). During this investigation the low-speed wind tunnel was operated in closed loop mode. Furthermore, a motion simulator is used in order to position the JBC hull model accurately in the wind tunnel, see Figure 3.

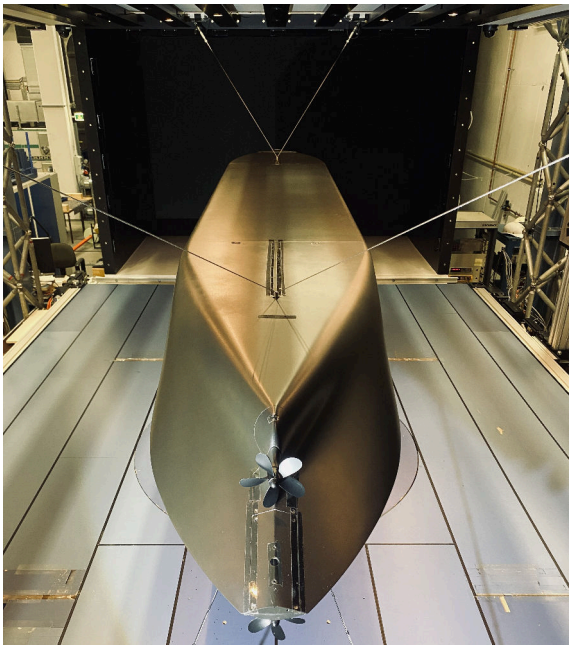

Figure 3: Double hull model of JBC mounted on the motion simulator

Tomographic Particle Image Velocimetry System

The measurement campaign of the double-body model was carried out using a Tomographic Particle Image Velocimetry System (T-PIV). It is particularly worth mentioning that by using T-PIV it is possible to measure a complete coherent three-dimenional volume and thus to determine all three components of the vorticity vector. The main components of the system are four cameras and a focused laser which illuminates the measurement volume. The laser is generated by a 40 mJ dual cavity Nd:YLF-laser (Photonics Industries). The four cameras are able to capture frames at a sampling frequency of 1.1kHz. The used sampling frequency is 500Hz, since double frames are needed. Di-Ethyl-Hexyl-Sebacat (DEHS) is used by the Laskin type droplet generator for the generation of seeding particles, which are injected downstream the test section. LaVision GmbH provided the post-processing software, which computes the quantities in the flow field. The volume has the extension of approximately 6mm x 310mm x 120mm. Due to the relatively small size of measured volumes, three windows are overlapped to one result array. The final measurement volume has the extent of 4.4mm x 307mm x 220mm with a meshsize of 1.1mm. The physical quantities are normalized in the following way:

- Distance by L_{pp}
- Velocity by u_∞
- Vorticity by u_∞/L_{pp}
- Turbulent Kinetic Energy by u_∞^2
- Wall Shear Stress and Pressure by $0.5\rho u_\infty^2$
- Force and Thrust by $0.5\rho u_\infty^2 A$

Measurement planes

The measurement planes used in the paper are summarized in Table 3.

Table 3: Measuring sections

Name	Position [–]	Description
S4	0.0157 L_{pp}	Propeller plane
S7	0.0000 L_{pp}	Aft Perpendicular (AP)
S7'	-0.0193 L_{pp}	Transom stern
FSV00	0.0000 L_{pp}	Fore-body side vortex (S7)
FSV10	0.1000 L_{pp}	Fore-body side vortex
FSV20	0.2000 L_{pp}	Fore-body side vortex

Measurement results

The results obtained in the wind tunnel to validate the CFD simulations in the ABV region are shown in Figures 4 (velocity u_x), 5 (vorticity ω_x) and 6 (TKE). A strongly delayed wake is recognizable in the propeller plane S4 which is characterized by the detachment of the ABV. A roll-up mechanism occurs, as can be seen from the vorticity. In the area of high gradients of velocity, increased TKE occurs.

In addition, measurements were conducted to capture the details of the flow of the FSV. The flow characteristics of ABV and FSV are shown in Figures 7, 8, 9 and 10 in the measurement plane positioned at the aft perpendicular. The results consist of several measurement windows which are superimposed.

Force measurements have also been taken during the studied setups. The hull forces were measured with a 6-component balance. In addition, the thrust of the propeller was measured. The measured values for the hull without appendages are summarized in Table 4.

A detailed insight into the performed PIV measurements is given in Sahab, et al. (2022) where the results of the measurements are comprehensively summarized.

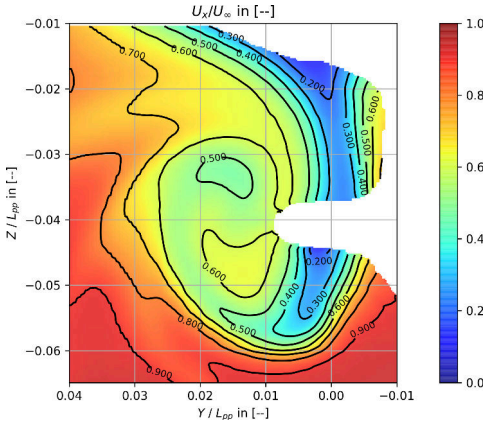

Figure 4: Measurement results, propeller plane S4, static drift, u_x

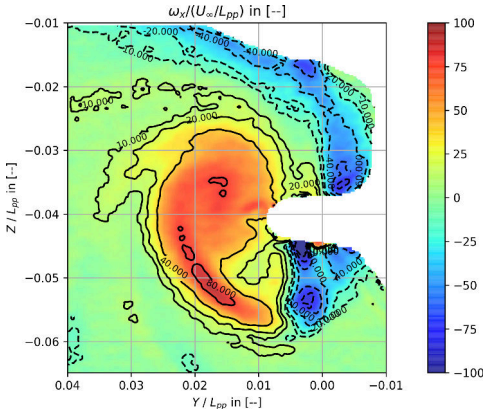

Figure 5: Measurement results, propeller plane S4, static drift, ω_x

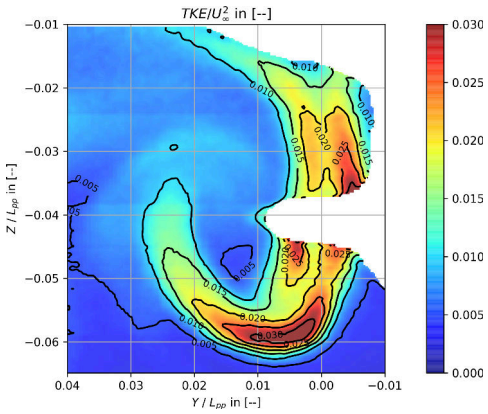

Figure 6: Measurement results, propeller plane S4, static drift, TKE

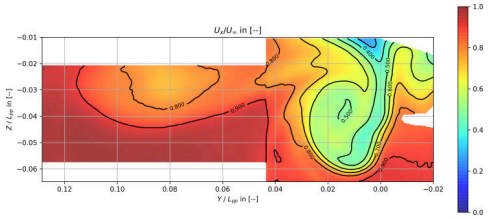

Figure 7: Measurement results, aft perpendicular S7, static drift, u_x

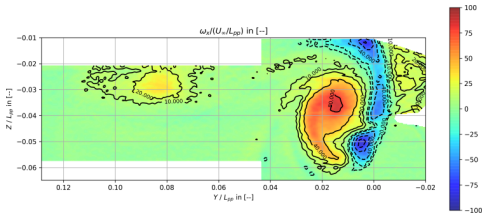

Figure 8: Measurement results, aft perpendicular S7, static drift, ω_x

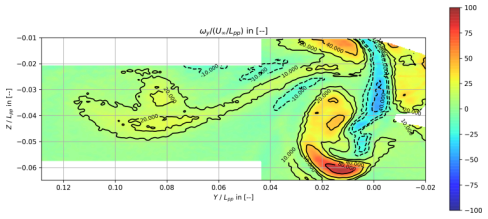

Figure 9: Measurement results, aft perpendicular S7, static drift, ω_y

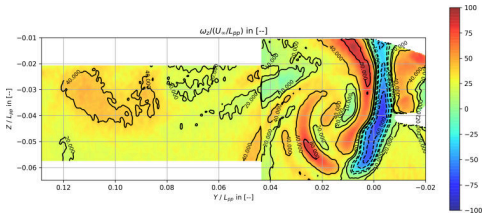

Figure 10: Measurement results, aft perpendicular S7, static drift, ω_z

Table 4: Measured longitudinal, transverse force and yaw moment

$c_{t,x}$	$c_{t,y}$	$m_{t,z}$
-6.51E-03	1.15E-02	3.89E-03

NUMERICAL INVESTIGATION

Numerical simulations are conducted for the JBC hull with and without propeller. In the framework of this study, the influence of five different grid sizes as well as a selection of various turbulence models on the vortical structures are evaluated. This approach allows the separation of the influence of spatial resolution from differences due to the turbulence model used. The mesh size ranges from 5M to 32M cells without propeller and around 50M cells with propeller.
In the simulations of the drift motion without propeller, the flow is investigated with respect to the local velocity, the vorticity as well as the TKE. Based on this, simulations with an active propeller are performed for positive and negative drift as well as for straight-ahead condition.

Setup

The simulations presented in this paper are conducted using Siemens PLM's finite volume CFD solver starCCM+. The turbulence closure problem is treated with Menter's two equation k-ω-SST model and is used in all RANS, DDES and IDDES simulations. The Courant-Number is kept under 1 in order to properly capture the dynamics of the vortex structures. The temporal discretization is realized by a second-order implicit unsteady solver. The convective terms of momentum equation are discretized by a second-order upwind scheme which is also used for convective terms of the applied k-ω-SST model in RANS. A hybrid second-order upwind/bounded-central scheme is used for modeling the convection terms of the DDES/IDDES approaches. The viscous sub-layer is part of the discretized domain, wall functions are therefore not necessary. The average Y^+-number is kept around 0.5. The timestep size is set to $\frac{1}{n_p \cdot 640}$ so that the propeller rotation advances 0.5625deg per timestep.

Boundary Condition

The boundary conditions of the simulated domain are set up as shown in Table 5. According to the EFD investigations, the JBC hull is modelled with a symmetry plane at the free water surface.

Table 5: Boundary Conditions within the Domain

Boundary	Condition	Value
x_{min}	pressure outlet	-
x_{max} y_{min} y_{max} z_{min}	velocity inlet	$u_x = u_\infty \cdot \cos(\beta)$ $u_y = u_\infty \cdot \sin(\beta)$ $I_t = \frac{u'}{u_\infty} = 0.01$ $\frac{\mu_t}{\mu} = 10$
z_{max}	symmetry	waterplane

Computational mesh

The simulation domain is discretized using the unstructured hex-dominant grid (trimmer mesher). Within the mesh study, 5 different mesh sizes has been used. The discretization of the unappended JBC hull counts from 5M up to 32M cells. Grid *G1* is the coarsest and *G5* the finest grid. The cell number count is approximately: 5M, 7M, 12M, 21M, 32M. An overview of the whole simulation domain is given in Figure 11. The flow region including ABV in the aft domain as well the FSV region are locally refined in order to increase the spatial accuracy.

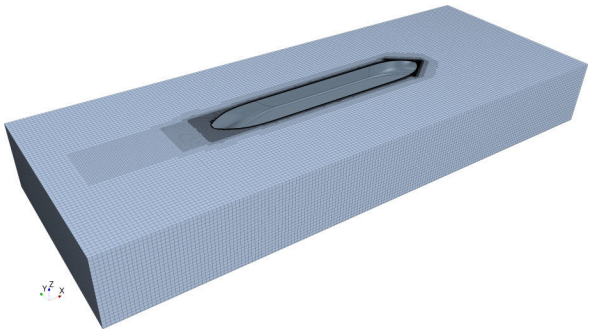

Figure 11: Computational domain of the JBC hull

A detailed view of computational mesh cells of a certain refinement level is displayed for the finest mesh discretization G5, see Figure 12. The refinements are important to accurately capture the wake of the hull and the FSV structure. The discretization in the measurement planes *S1* (in front of propeller) and *S4* (propeller plane) are shown in Figure 13. The coordinate system is located in the longitudinal symmetry plane at the aft perpendicular, the vertical z-axis points upwards and the transverse y-axis to port side.

(a) $\Delta x = 0.064\% L_{pp}$ **(b)** $\Delta x = 0.032\% L_{pp}$

Figure 12: Mesh cells of equal refinement levels

STATIC DRIFT CONDITION WITHOUT APPENDAGES

Validation

The validation of the numerical model is determined by conducting simulations for the static drift condition

(a) 0.05 L_{pp} (S4) **(b)** 0.0157 L_{pp} (S4)

Figure 13: Cross-section through the computational mesh

without appendages. Therefore, the force coefficients for longitudinal and transverse force and the yaw moment are analyzed. While IDDES solutions are computed on all five grids, RANS and DDES simulations are conducted on three grids. The results for the longitudinal and transverse force coefficients ($c_{t,x}$ and $c_{t,y}$) and yaw moment coefficient m_z are summarized in Table 6. While the RANS and DDES simulations show good convergence of the forces and moments, the IDDES simulation shows no convergence of the transverse force. However, this behavior is not observed for the longitudinal force and the yaw moment. An increased sensitivity of the IDDES method to the varied grid size is noticed.

Additionally, the resistance coefficients are split into pressure and shear contribution in Table 7. The changing resistance predicted by IDDES has its origin in the pressure component, as shear forces converge very fast in all cases.

Disregarding the IDDES simulations on coarse grids, only a small scatter of the computational results can be seen. The measured forces of the JBC in the wind tunnel of TUHH are used as reference. The discrepancies for the longitudinal forces lie in the range of 11-14%, 10.5-11.6%, 12-12.9% for IDDES, DDES and RANS respectively, whereas for the transverse force - 1-13%, 0-3%, 2-3% for IDDES, DDES and RANS. Only in the prediction of the yaw moment, there is a larger discrepancy in the EFD results compared to RANS and IDDES discernible.

For a more thorough analysis of the cause of the differences between the forces predicted by RANS and IDDES on G5, as clearly seen in Table 7, the distributions of the longitudinal and transverse force coefficients ($c'_{t,x}$, $c'_{t,y}$) along the hull are plotted (see Figures 14 and 15). Obviously, the discrepancies between the methods come from the stern area. Together with the force decompositions presented in Table 7, these plots support the assumption that IDDES solution on coarse grids suffered from modeled stress depletion (MSD).

At the same time, in the region $0.05 < x/L_{pp} < 1.025$, the IDDES and RANS distributions of $c'_{t,x}$ agree very well, including the region of FSV formation. This may

Table 6: Grid convergence analysis for different turbulence modelling approaches, modelling Error E%D (r: RANS k-ω-SST, i: IDDES k-ω-SST, d: DDES k-ω-SST), the uncertainity of the measured hydrodynamic forces is less than 0.15%

Case	$c_{t,x}$	$c_{t,y}$	$m_{t,z}$	E%D [%]
i / G1 / 5M	-6.50E-03	1.45E-02	3.45E-03	00.09 26.00 -11.44
i / G2 / 7M	-6.24E-03	1.38E-02	3.68E-03	04.15 19.83 -5.40
i / G3 / 12M	-5.68E-03	1.25E-02	4.24E-03	12.78 08.35 9.00
i / G4 / 21M	-5.78E-03	1.30E-02	4.04E-03	11.21 13.04 3.86
i / G5 / 32M	-5.59E-03	1.17E-02	4.56E-03	14.15 01.30 17.10
d / G1 / 5M	-5.75E-03	1.15E-02	4.43E-03	11.61 -00.09 13.75
d / G3 / 12M	-5.83E-03	1.19E-02	4.26E-03	10.75 04.26 9.51
d / G5 / 32M	-5.81E-03	1.20E-02	4.24E-03	10.45 03.65 8.87
r / G1 / 5M	-5.73E-03	1.13E-02	4.53E-03	12.04 -02.17 16.32
r / G3 / 12M	-5.69E-03	1.11E-02	4.56E-03	12.61 -03.30 17.22
r / G5 / 32M	-5.67E-03	1.13E-02	4.51E-03	12.89 -02.09 15.94
mean	-5.84E-03	1.22E-02	4.20E-03	10.29 -06.09 8.61

Table 7: Pressure and shear force contribution for different meshes (r: RANS k-ω-SST, i: IDDES k-ω-SST, d: DDES k-ω-SST)

Case	$c_{t,x,p}$	$c_{t,x,v}$	$c_{t,y,p}$	$c_{t,y,v}$
i / G1 / 5M	-3.268E-03	-3.236E-03	1.427E-02	2.211E-04
i / G2 / 7M	-2.937E-03	-3.304E-03	1.356E-02	2.215E-04
i / G3 / 12M	-2.339E-03	-3.339E-03	1.224E-02	2.201E-04
i / G4 / 21M	-2.468E-03	-3.312E-03	1.279E-02	2.172E-04
i / G5 / 32M	-2.276E-03	-3.313E-03	1.143E-02	2.173E-04
d / G1 / 5M	-1.880E-03	-3.874E-03	1.118E-02	3.093E-04
d / G3 / 12M	-1.957E-03	-3.873E-03	1.161E-02	3.071E-04
d / G5 / 32M	-1.944E-03	-3.866E-03	1.168E-02	3.084E-04
r / G1 / 5M	-1.825E-03	-3.896E-03	1.095E-02	3.088E-04
r / G3 / 12M	-1.781E-03	-3.908E-03	1.081E-02	3.126E-04
r / G5 / 32M	-1.765E-03	-3.906E-03	1.095E-02	3.131E-04

be attributed to the fact that the separations in the bow region (e.g. FSV formation) are geometrically defined and are not largely influenced by the MSD. Whereas in the stern region also the separations due to the adverse pressure gradient occur, which are highly sensitive to the turbulence characteristics upstream. A similar conclusion can be drawn for $c'_{t,y}$. The distributions from IDDES and RANS solutions agree well for $0.35 < x/L_{pp} < 1.025$, but starting from the end of the cylindrical body ($x/L_{pp} < 0.35$), the discrepancy increases (for the same reasons as discussed for $c'_{t,x}$).

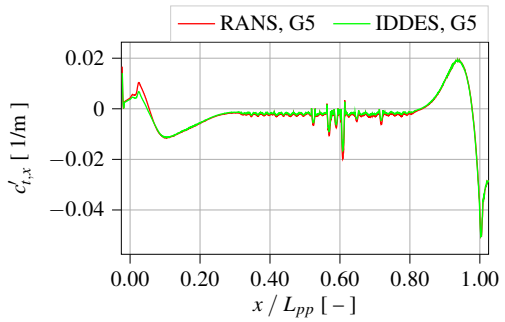

Figure 14: Longitudinal forces for different approaches, $+\beta$

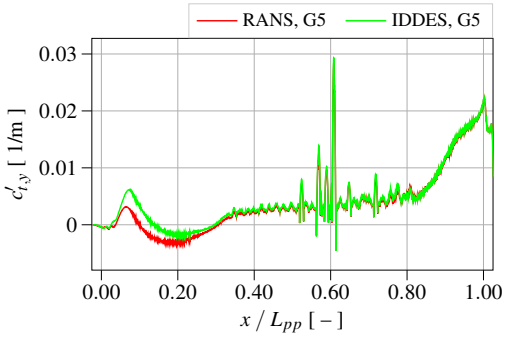

Figure 15: Transversal forces for different approaches, $+\beta$

Figures 72 (S4) and 73 (S7) show the computational results of the three methods (each on the finest grid) compared to the measurement results. The black lines correspond to the iso-lines of the measurement. The color scale and the lines in light gray correspond to the simulation. The basic vortex structure is reproduced by all methods, however in terms of details RANS gives a better agreement of the iso-lines with EFD than DDES/IDDES (see e.g. Fig. 72a). The value of the vorticity in the ABV is higher in the case of DDES and IDDES, compared to RANS. Large differences are observed for TKE also. While the TKE level and structure are similar for RANS and DDES, the IDDES method predicts higher TKE values.

Flow field analysis

In the following, the flow field around the JBC hull is discussed in detail. The time-averaged vorticity at selected levels as well as the wall friction and its implied direction are shown in Figure 16 (RANS k-ω-SST) and 17 (IDDES k-ω-SST). It can be seen that for the hybrid methods, detachment already in the fore-body leads to more complex flow conditions. Separation is also indicated by low wall shear stresses. In addition, the FSV induces high shear stress in the near-body region due to increased velocities and thus also negative pressure. The vorticity is more pronounced, as can be seen from a higher shear stress using IDDES, see Figure 17 .

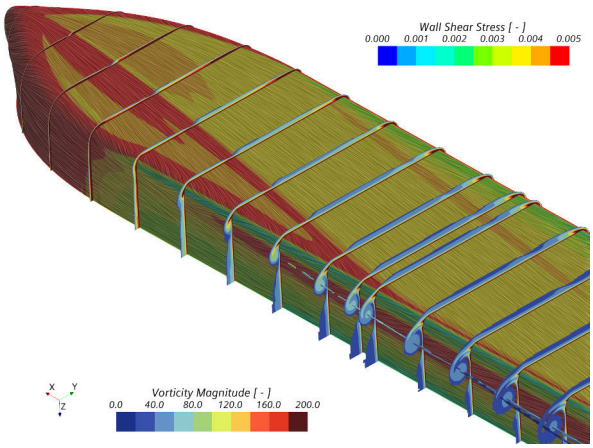

Figure 16: Evolution of FSV and ABV at foreship region, RANS k-ω-SST, $-\beta$

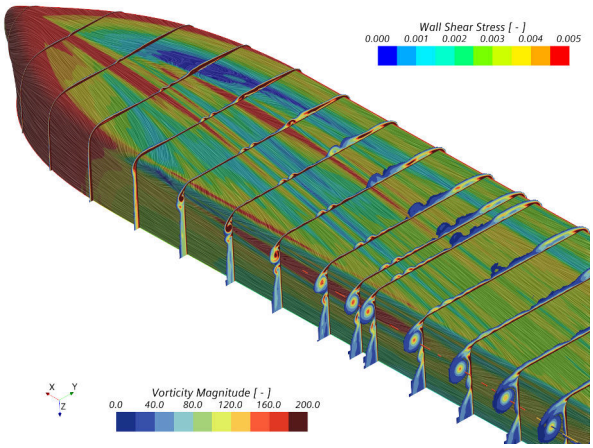

Figure 17: Evolution of FSV and ABV at foreship region, IDDES k-ω-SST, $-\beta$

The time-averaged position of the vortex core has been determined using the helicity method by Levy, et al.

(1990) and is shown in both figures. The onset of detachment is visible in the planes and illustrates how the vortex gains energy downstream by suction of the detaching flow.
Similar behavior is observed for ABV, although in this case the process is further enhanced by the taper of the hull. In addition, it is noticeable that in the case of DDES, the interaction of the detached FSV and the forming ABV can be observed downstream. In general, the hybrid approaches lead to higher vorticity, with more bunching obtained in the case of IDDES (Figure 19), whereas the DDES approach leads to a kind of smearing of calculated vorticity, see Figure 20.

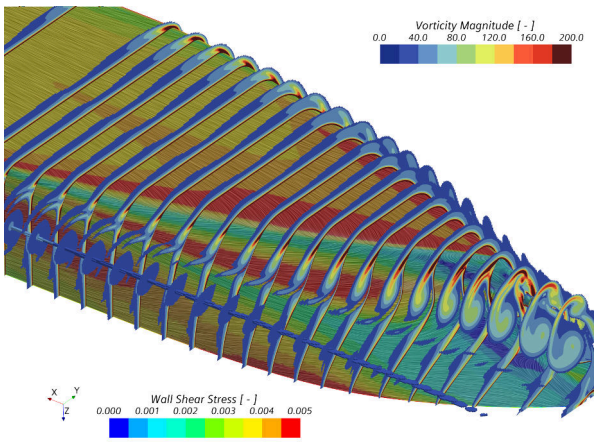

Figure 18: Evolution of FSV and ABV at stern region, RANS k-ω-SST, $-\beta$

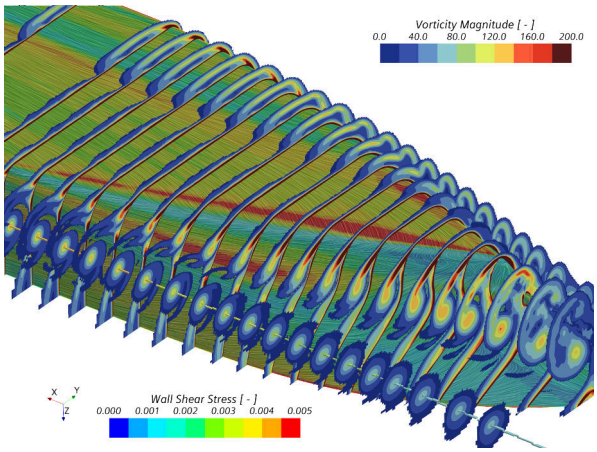

Figure 19: Evolution of FSV and ABV at stern region, IDDES k-ω-SST, $-\beta$

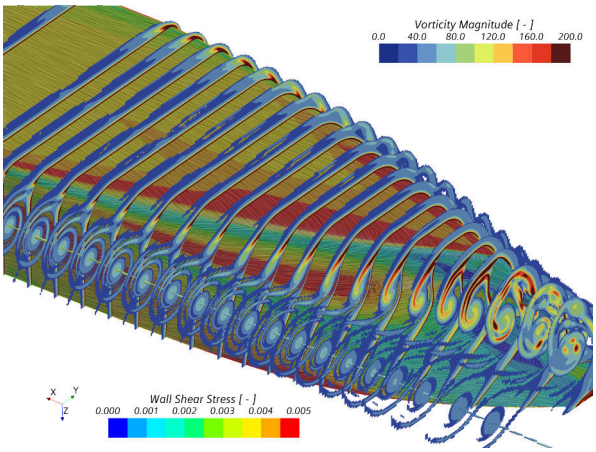

Figure 20: Evolution of FSV and ABV at stern region, DDES k-ω-SST, $-\beta$

Fore-Body Side Vortex Analysis

In the following, the FSV is analyzed to quantify the influence of the turbulence modeling on the vortex features as well as to investigate its interaction with the propeller. As described in Figure 16 the vortical structure arises in the fore-ship region and gains its strength by further detaching flow downstream from its origin. In general, all used turbulence models and grids are able to predict the location of FSV and the axial velocity component. Further validation is conducted by using wind tunnel test results. Within a measurement campaign of the JBC hull at static drift the FSV has been investigated using tomographic PIV up to $0.2L_{pp}$ upstream from aft perpendicular. The measurement setup in the tunnel wind facility at TUHH is shown in Figure 21.

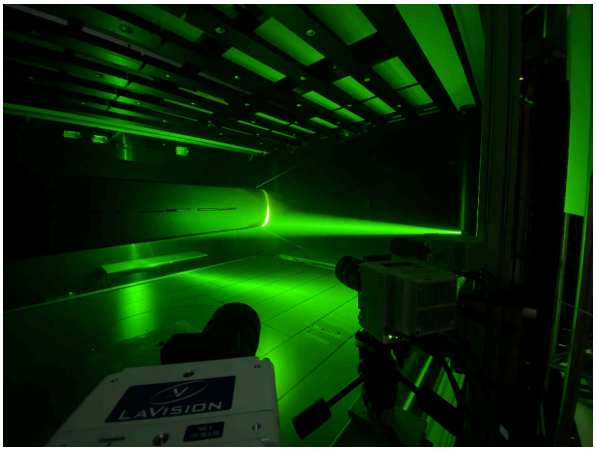

Figure 21: Tomographic PIV setup for static drift JBC measurements, TUHH wind tunnel

The location of measurement planes are shown in Figure 22. These planes are located with an increment of $0.05L_{pp}$ from aft perpendicular. In the DDES simulation, the vortex structure is visible in detail. Increased vorticity between the FSV and ABV shows that there is a considerable interaction between the two vortices and the flow is strongly influenced by the complex vortical structure developed.

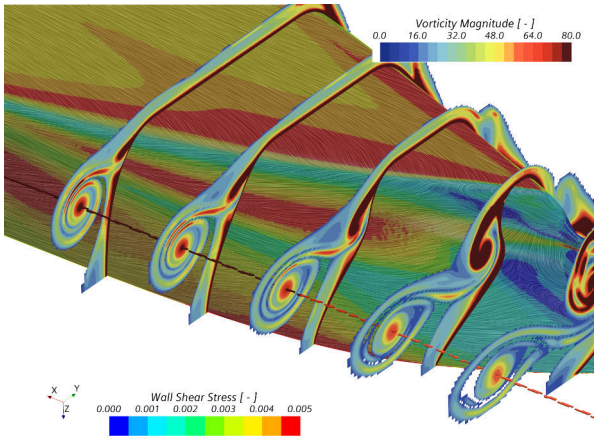

Figure 22: Vorticity magnitude and the wall shear stress at investigated measurement planes, DDES k-ω-SST

In the following, the position of the vortex core and its flow quantities are analyzed. The position in y- and z-direction is summarized in Figures 23 and 24. The results of the measurement are shown in black points. In the transverse direction, the agreement of the IDDES simulation on fine grids with the measurement results is good. Beyond that, however, the deviations between the methods are low.

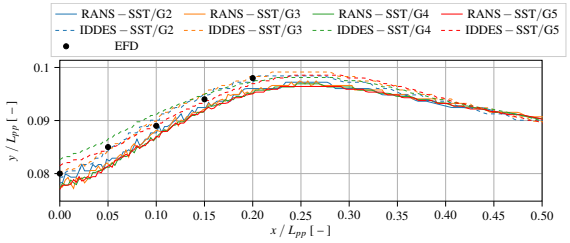

Figure 23: Transverse location of the vortex core region, static drift condition

The axial velocity component in the vortex core direction is captured very well by RANS and agrees with wind tunnel measurements, see Figure 25. The IDDES solution also converges to the wind tunnel results with increasing grid resolution.

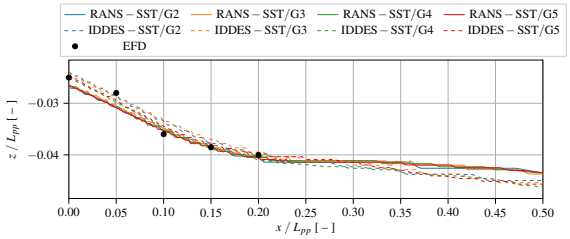

Figure 24: Vertical location of the vortex core region, static drift condition

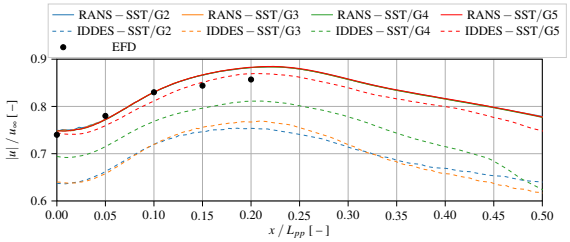

Figure 25: Axial velocity component in the vicinity of the vortex core region, static drift condition

RANS, on the other hand, massively underestimates the axial vorticity, while IDDES predicts it in agreement with the measurement results, see Figure 26. The local grid size is 1.1mm in the EFD measurements and 2.2mm in CFD on finest mesh.

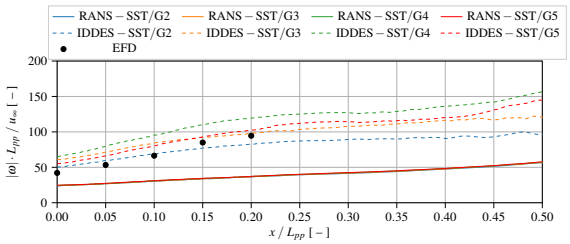

Figure 26: Axial vorticity in the vicinity of the vortex core region, static drift condition

Furthermore, convergence for the TKE level in the vortex core using IDDES is only achieved with very fine grids, shown in Figure 27. Unfortunately, due to the lack of TKE measurement results, a validation is not possible, see Sahab, et al. (2022).

A detailed comparison of numerically and experimentally estimated flow field quantities in the immediate vicinity of the FSV is given in Figures 74 and 75 as well as 73 (on finest grids). Measurement results are shown as a black contours. Overall, the agreement across all computational methods is good. As already mentioned, there are significant differences especially for the vorticity. While RANS simulations tend to underestimate, IDDES results

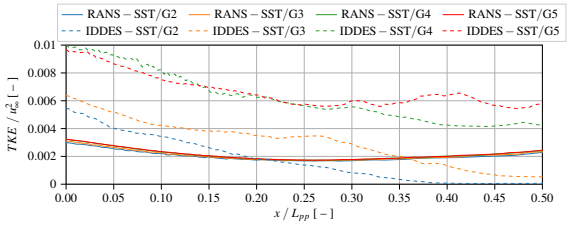

Figure 27: TKE level in the vicinity of the vortex core region, static drift condition

have pronounced maxima in the vortex core. The DDES approach seems to be able to predict the details of the vortex structure more accurate than IDDES and RANS near the FSV vortex core (see ω_y and ω_z, further minima and maxima outside the vortex core).

In addition, Figure 28 summarizes the results of the FFT of the vortex core position in the y and z directions. The change in the position of the vortex has no dominant frequency in both directions. The behavior shows random disturbance similar to signal noise. This is valid for all investigated positions of the FSV. The amplitudes of the high-frequency components of the vortex core motion keep increasing downstream. This is valid for the lower frequency range less than 500Hz.

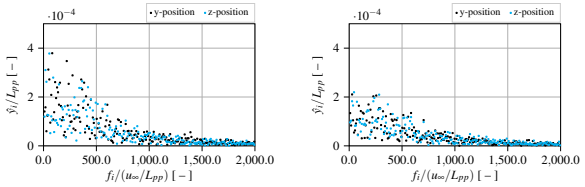

(a) $x = 0.2L_{pp}$ **(b)** $x = 0.4L_{pp}$

Figure 28: FFT analysis of FSV vortex position

To illustrate the influence of the vortex structures on the flow on the hull, the variance of the surface pressure and the variance of the wall shear stress determined from the IDDES results are shown in Figures 29a and 29b. Areas where these values increase are particularly affected by the unsteadiness of the flow around the hull. Especially in the region of incipient detachment of the FSV, a local increase in the variance of surface pressure indicates that the detachment behavior is already strongly unsteady at the onset. The figures show that there is a time-dependent shift in the detachment point of the FSV. However, this area is limited locally and relatively small compared to the vortex size. Likewise, the variance is increased and pronounced downstream, indicating an interaction of the vortex with the hull. This is primarily caused by the detachment of the ABV at the aft shoulder.

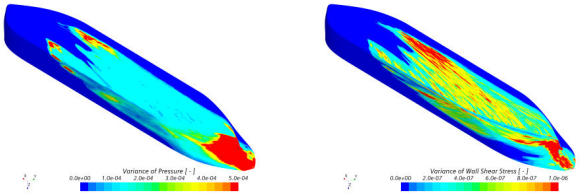

(a) Surface Pressure **(b)** Wall Shear Stress

Figure 29: Variance of surface pressure and wall shear stress at static-drift ($-\beta$)

STATIC DRIFT CONDITION WITH PROPELLER

Description of flow field

The interaction of the propeller with the ship hull has been extensively studied, however off-design conditions are rarely examined. This is the motivation to investigate the propeller in the wake of the JBC under drift condition. It was obvious, that two different states needed to be investigated: positive ($+\beta$, the bow of the ship directed to the port side) and negative drift ($-\beta$, the bow of the is directed to the starboard side). Since the wake field varies considerably depending on the drift angle, the propeller will work at different operating points at the same drift angle, depending on whether the drift angle is positive or negative. The propeller rotation speed n_p is kept constant at 125 1/s in all simulations. The different wake fields result in a variation of the inflow angles to the propeller blades which has a similar effect as different advance ratio J coefficient for each case.
Figure 30 shows the velocity magnitude field in a horizontal plane at static drift condition without propeller, Figure 31 with propeller. The plane is positioned at the same height as the propeller rotation axis. Due to the induced velocity field of the propeller and an asymmetrical wake, a low and a high-speed area are generated. A shear flow region becomes visible and the ABV interacts with the propeller tip vortices. Additionally, the induced velocity by the propeller induces a lower pressure region upstream at the rear shoulder.

The iso-surface of Q-criterion ($Q = 2500\ 1/s^2$) demonstrates the influence of the drift angle on the behavior of the flow. The rotation direction of the vortex system is strongly influenced and merged with the propeller slipstream (see Figure 32 and 33). The ABV detaches from the hull slightly more downstream which is caused by the propellers suction.

Computations have been conducted using RANS and IDDES. Simulations with DDES were not performed, since the influence of high TKE obtained by IDDES needs to be investigated at this point. Figure 34 gives an impression of the unsteady vortex structure behind the

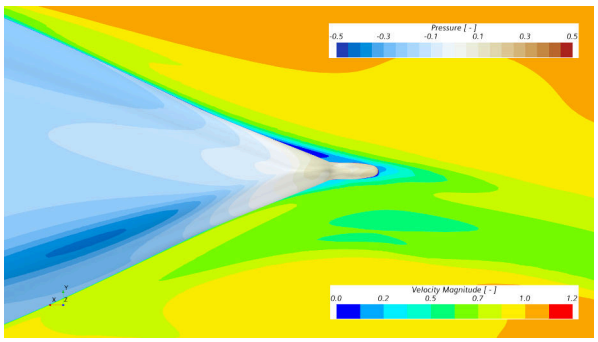

Figure 30: Velocity magnitude field and pressure distribution on the after body at static drift (unappended, $-\beta$)

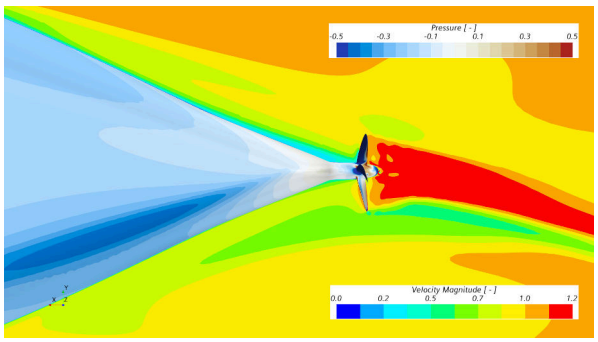

Figure 31: Velocity magnitude field and pressure distribution on the after body at static drift (with propeller, $-\beta$)

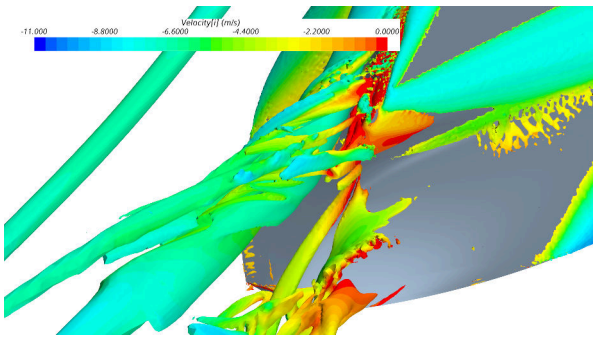

Figure 32: Q-criterion iso-surface (2500 $1/s^2$) with axial velocity component, DDES k-ω-SST without appendages, $-\beta$

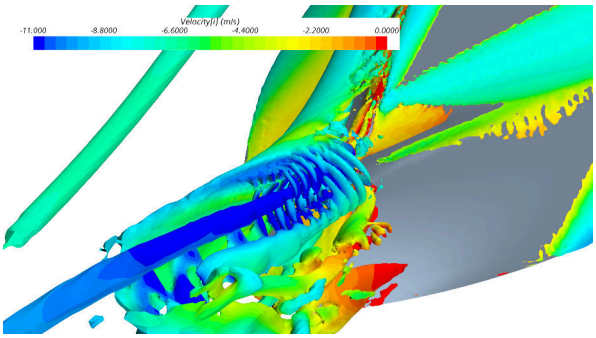

Figure 33: Q-criterion iso-surface (2500 $1/s^2$) with axial velocity component, DDES k-ω-SST with propeller, $-\beta$

propeller. RANS results provide a global impression of the flow conditions. Therefore, the flow field is averaged 5 times per revolution (5-bladed propeller). Then the tip vortex of the propeller and its deformation due to the asymmetric wake also becomes visible, see Figure 35.

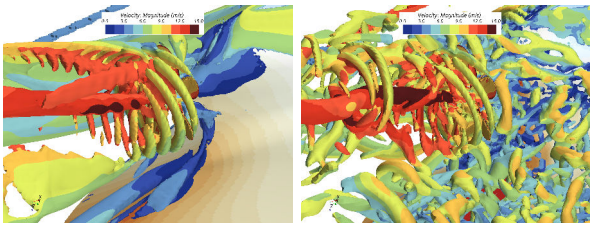

(a) RANS SST **(b)** IDDES SST

Figure 34: Unsteady Q-criterion iso-surface (2500 $1/s^2$), $-\beta$

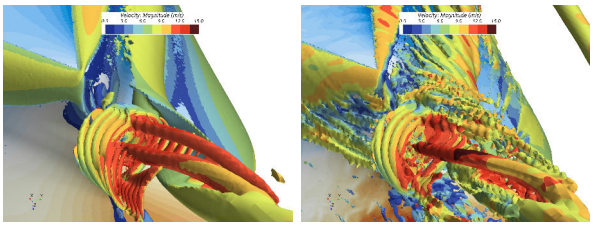

(a) RANS SST, $+\beta$ **(b)** IDDES SST, $+\beta$

Figure 35: Phase averaged Q-criterion iso-surface (2500 $1/s^2$), $+\beta$, RANS/IDDES k-ω-SST

The influence of drift angle is shown in Figure 36. The interaction of ABV with the propeller depends highly on the rotation direction of the vortex flow. At positive drift ABV's rotation direction is the same as the propeller rotation direction, while at negative drift they are contra-rotating. The result is a different flow structure downstream.

A more detailed view of flow structures for both cases is

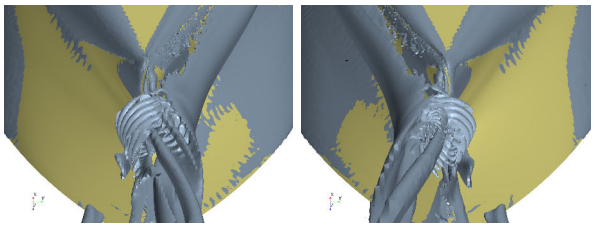

(a) $+\beta$ **(b)** $-\beta$

Figure 36: Q-criterion iso-surface , RANS k-ω-SST

shown in Figure 37. The vorticity magnitude is shown at different cross sections. It can be seen that the location of the detachment of ABV appears to be different at the rear shoulder. Furthermore, the shapes of the closed vorticity rings differ in the slipstream of the propeller.

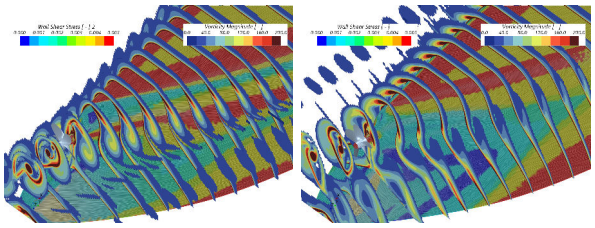

(a) $+\beta$ **(b)** $-\beta$

Figure 37: Vorticity planes, RANS k-ω-SST

Comparison with experimental data

Flow field quantities in the measured planes

The flow field is validated by comparison of the time-averaged velocity and vorticity field. Figure 76 shows the results of measurement plane S7' which is placed at the transom stern of JBC hull. The results show the axial velocity component and the three components of the vorticity vector, for $+\beta$ and $-\beta$ respectively. Agreement between the RANS solution and EFD is observed in all cases. It is particularly noteworthy that even the details of ω_y and ω_z are predicted. Likewise, the IDDES results show minor deviations of measurements, see Figure 77. The velocities calculated by both methods are largely in agreement with the measurement. Differences are mainly found in the vorticity, see e.g. 76f and 77f. Also Figures 76d and 77d show a deviating position of the maxima for ω_x. Furthermore, it is shown that the RANS method is not able to reproduce TKE, whereas IDDES predicts the correct level of TKE, see Figure 78.

Forces and propulsion

In this section, the forces and the propulsion characteristics of the investigated test cases are discussed. It is important to keep in mind that the simulated test case does not represent an equilibrium of the thrust force and the model resistance. The rotation speed of the propeller is set constant to 125 1/s over all test cases. Therefore, the propeller cannot compensate the entire drag force. However, the thrust force and the propeller torque will be both susceptible to any changes in the wake of the model. In order to analyze the interaction between the propeller and the hull, the Taylor wake fraction w and the thrust deduction fraction t for different cases are compared. In Table 8, addition, the straight-ahead case is selected as a reference for the comparison. The coefficients of the propeller side force k_ε, the thrust k_T and the torque k_Q are considerably larger at a positive drift angle compared to the corresponding values at a negative drift angle. The magnitudes of k_T and k_Q have decreased for the positive and negative drift angles compared to the straight-ahead condition, but the decreases for the negative drift case is drastic. The thrust loading of the propeller is relatively small ($C_{th} \approx 1$) compared to the thrust loading of the full scale condition with a $C_{th} \geq 2$.

In addition, the total resistance coefficients c_T and the wake fraction w are summarized in Table 9. The wake is determined for the axial velocity component in a similar manner as under straight-ahead condition: $w = 1 - \frac{\overline{u}_x}{u_\infty}$, where $\overline{u}_x$ is the mean nominal wake velocity within the propeller area. As expected, the total drag increases for both drift conditions compared to straight ahead case and at the same time w decreases because nearly half of the propeller disc area is exposed to the free, undisturbed flow.

Table 8: Comparison of the thrust k_T, the k_ε, and the torque k_Q coefficients for positive and negative drift (r: RANS k-ω-SST, i: IDDES k-ω-SST)

Case	k_T	k_ε	$10k_Q$
0deg/EFD	2.35E-01	-	-
0deg/r	2.24E-01	-5.09E-03	-3.09E-01
$+\beta$/EFD	2.20E-01	-	-
$+\beta$/r	2.14E-01	1.58E-02	-3.07E-01
$+\beta$/i	2.03E-01	1.30E-02	-2.92E-01
$-\beta$/EFD	1.95E-01	-	-
$-\beta$/r	1.63E-01	-1.16E-02	-2.48E-01
$-\beta$/i	1.60E-01	-1.06E-02	-2.43E-01

A detailed investigation of the distribution of longitudinal and lateral force coefficients along the longitudinal axis of the ship provides further insight regarding the reason for

Table 9: Comparison of total resistance coefficient c_T and wake fraction w (r: RANS k-ω-SST, i: IDDES k-ω-SST)

Case	c_T	w
0deg/EFD	-6.12E-03	-
0deg/r	-5.02E-03	5.80E-01
$\pm\beta$/EFD	-6.51E-03	–
$\pm\beta$/r	-5.71E-03	4.70E-01
$\pm\beta$/i	-5.65E-03	4.50E-01

the differences in forces. Figure 38 shows the comparison of the longitudinal force coefficient per ship length $c'_{t,x}$ for straight ahead condition and both drift cases. The peak in the area of the propeller is striking. This confirms the statement that a high thrust is generated by the propeller at positive drift condition.
The differences in the lateral force coefficient $c'_{t,y}$ become visible not only in the area of the propeller, but also upstream of the propeller, see Figure 39. With a positive drift angle, the difference to the straight ahead condition is almost twice as large compared to negative drift. For the negative drift case, the sign of the drift force coefficient has been reversed in Figure 39 for comparison purposes.

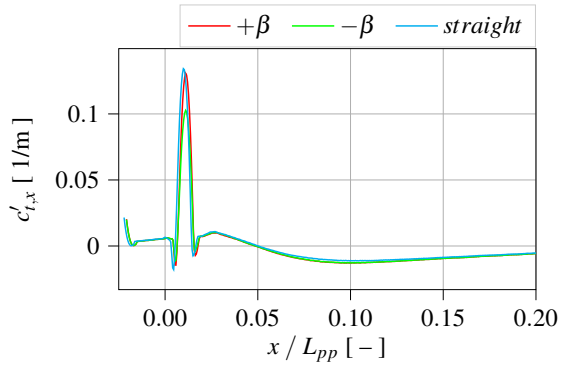

Figure 38: Longitudinal force coefficient, IDDES k-ω-SST, straight ahead, positive and negative drift

Figure 40 and 41 show a comparison of the calculated force coefficients using RANS and IDDES for the case of positive drift angle with and without propeller. As can be seen in the Figure 40, the differences in the longitudinal force coefficient $c'_{t,x}$ are small, only small deviations in $c'_{t,x}$ take place outside the propeller region. The largest differences are observed in $c'_{t,y}$, see Figure 41. Notably, the influence of the propeller on the lateral force is observed up to 30% of L_{pp} upstream in the results obtained by the IDDES approach, while this effect is observed only up to about 15% of L_{pp} in the RANS simulation.
Obviously, RANS and IDDES lead to quite different

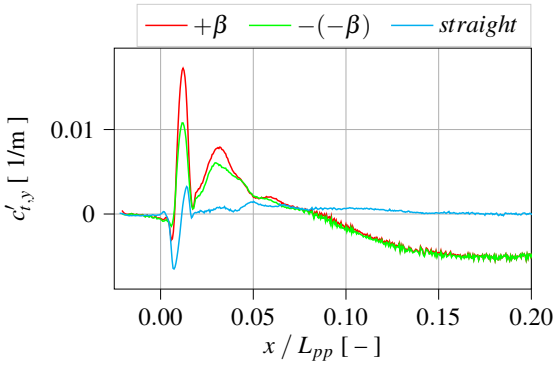

Figure 39: Transverse force coefficient, IDDES k-ω-SST, straight ahead, positive and negative drift

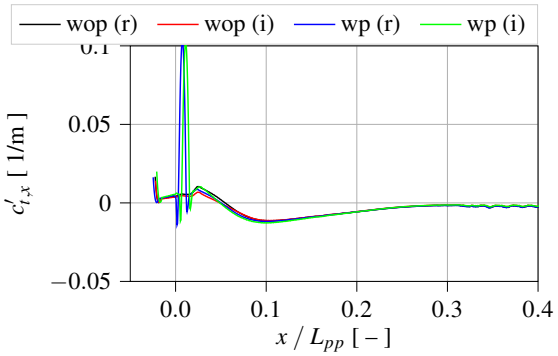

Figure 40: Longitudinal force coefficient, IDDES (i)/RANS (r) k-ω-SST, positive drift, with propeller (wp) and without propeller (wop)

results with regards to the propeller influence on the transversal force in the stern region. Figures 42a and 42b show the streamlines in the area of the aft. The streamlines reveal the different detachment mechanisms in the area of the aft ship between both approaches causing different TKE levels (see Figure 72). The ABV is more clustered within the RANS simulation. The flow calculated with IDDES is dominated by separation in the after body region, where higher velocities of streamlines are observed in the ABV.
The results of the RANS and IDDES calculations for positive and negative drift cases confirm the flow behavior described above, see Figures 43 and 44. To simplify the comparison, the sign of transverse force at negative drift is shown with the opposite sign. The progression of the transverse force upstream of the propeller is similar for both the positive and negative drift cases for each simulation approach individually. However, there is an agreement between both methods in the area of the propeller plane regarding each of the positive and negative drift case.

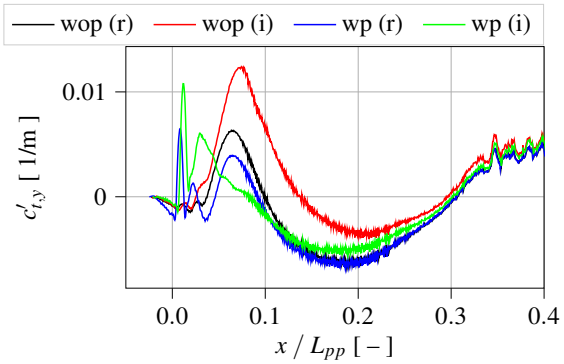

Figure 41: Transverse force coefficient, IDDES (i)/RANS (r) k-ω-SST, positive drift, with propeller (wp) and without propeller (wop)

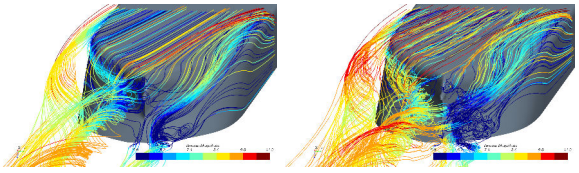

(a) RANS k-ω-SST **(b)** IDDES k-ω-SST

Figure 42: Streamlines in the aft-ship region, RANS/IDDES k-ω-SST, $-\beta$

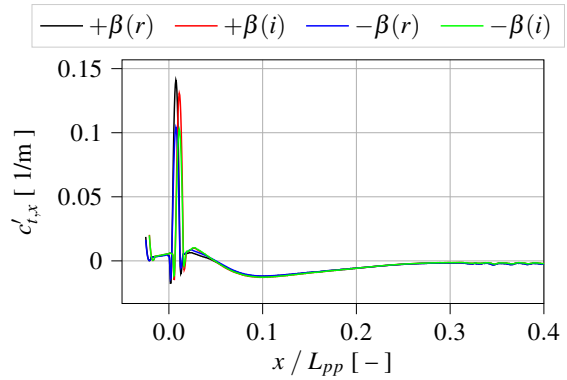

Figure 43: Longitudinal force coefficient, ship hull with propeller, positive and negative drift, RANS-SST (r) and IDDES-SST (i)

Propeller blade forces

The change in the thrust coefficient of a propeller blade during several revolutions for $+\beta$ and $-\beta$ is shown in Figure 45 and Figure 46 respectively. The results for straight-ahead condition is taken as a reference in both figures. Principally, the two cases show different characteristics. The IDDES method predicts larger

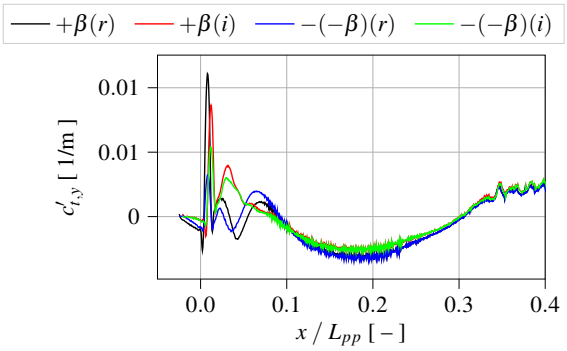

Figure 44: Transverse force coefficient, ship hull with propeller, RANS-SST, positive and negative drift, RANS-SST (r) and IDDES-SST (i)

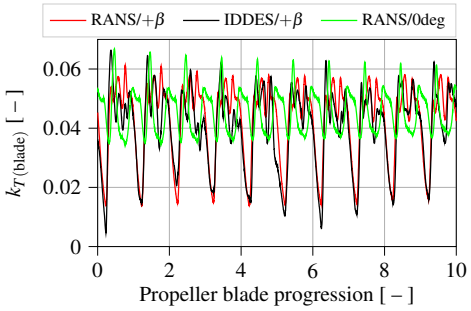

Figure 45: Thrust coefficient of a single propeller blade, RANS vs IDDES k-ω-SST, straight-ahead and positive drift

fluctuations of thrust as expected. This is also confirmed by the FFT analysis of the force curves. The first and second order of the thrust coefficient are clearly more pronounced in the drift case than in straight-ahead case. The forces of a single propeller blade during one revolution for different radial sections are shown for both positive and negative drift cases in Figure 49 and Figure 50 respectively. The differences of the propeller forces under different operating conditions are outlined. The section-wise thrust coefficients $k_{T\,(\mathrm{blade})}$ are calculated by means of phase-averaging of 20 propeller revolutions for each case. The 0deg deg corresponds to the 12 o'clock position. The propeller forces are analyzed alongside radial positions of the propeller blade in steps of 10% of the propeller radius. While the thrust reaches its maximum at about 150° and 360° in the negative drift case, it drops significantly between these values. Contrarily, there is no drop in thrust between 180° and 360° in the positive drift case. The highest contribution to the thrust is delivered between 0.75R and 0.85R.

In addition to the propeller blade forces, the thrust and torque coefficient time series for the entire propeller are shown, see Figures 51a (k_T) and 51b (k_Q).

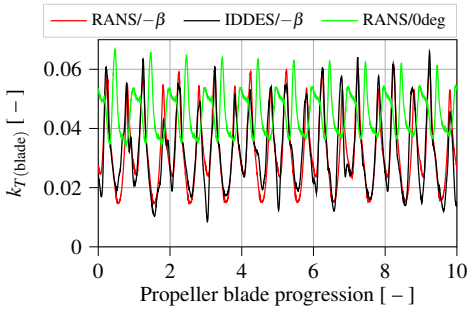

Figure 46: Thrust coefficient of a single propeller blade, RANS vs IDDES k-ω-SST, straight-ahead and negative drift

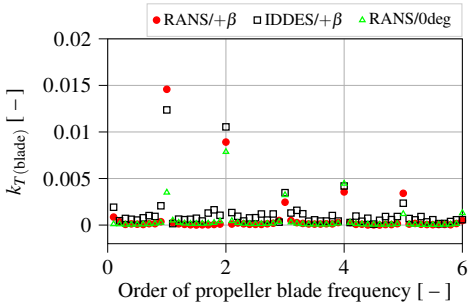

Figure 47: FFT analysis for the thrust force of a single propeller blade, RANS vs IDDES k-ω-SST, straight-ahead and positive drift

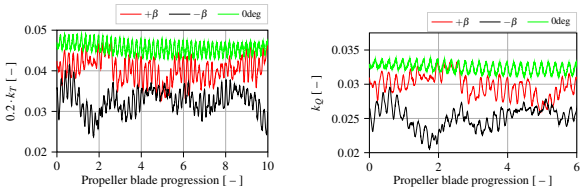

(a) k_T **(b)** k_Q

Figure 51: Thrust and torque coefficient of the entire propeller, IDDES k-ω-SST

The tangential force coefficient $k_{T,T}$ in the propeller fixed rotating coordinate system in the positive and negative drift cases is shown in Figure 52 and Figure 53 respectively. The tangential force correlates with the propeller thrust.

Additionally, the side force coefficient k_ε caused by the propeller blade during one revolution in both the positive and negative drift cases are shown in Figure 54 and Figure 55 respectively.
Figure 56 shows the radial distribution of the average axial force for each propeller blade $f_{x,i}$ calculated by IDDES. The average total thrust force $f_{x,i}$, the contribution of the pressure side $f_{x,i,p}$ and the contribution of the suction side

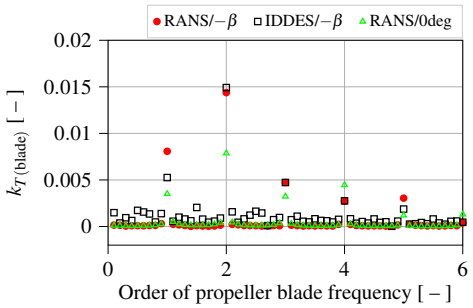

Figure 48: FFT analysis for the thrust force of a single propeller blade, RANS vs IDDES k-ω-SST, straight-ahead and negative drift

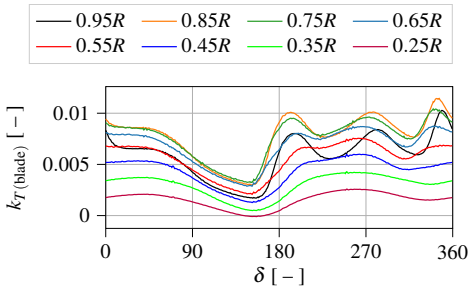

Figure 49: Axial thrust force coefficient of a single propeller blade during one period, $+\beta$

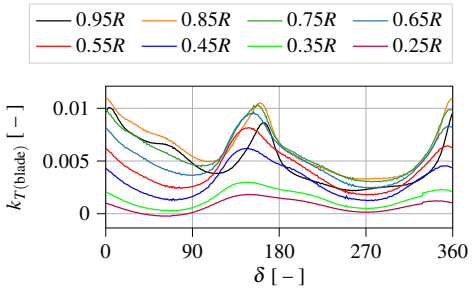

Figure 50: Axial thrust force coefficient of a single propeller blade during one period, $-\beta$

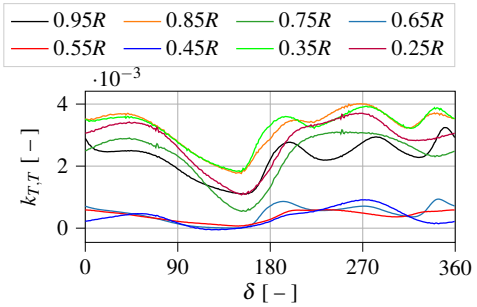

Figure 52: Tangential force coefficient of a single propeller blade during one period, $+\beta$

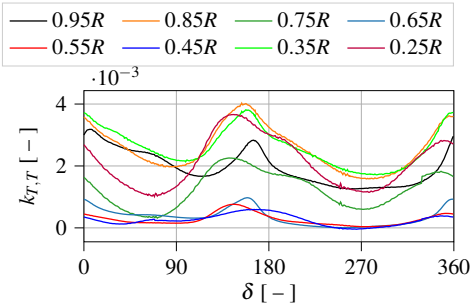

Figure 53: Tangential force coefficient of a single propeller blade during one period, $-\beta$

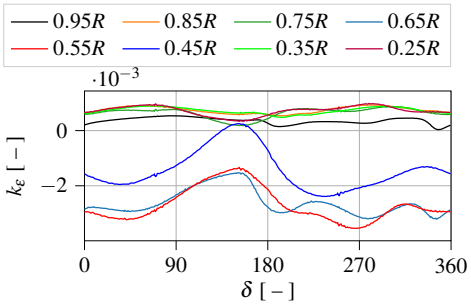

Figure 54: Ship fixed transversal force induced by a single propeller blade during one period, $+\beta$

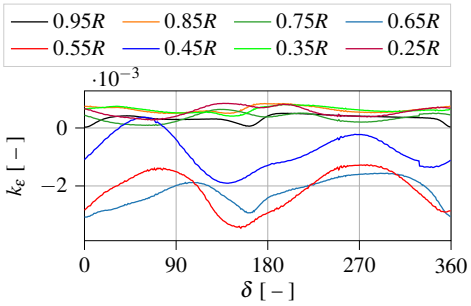

Figure 55: Ship fixed transversal force induced by a single propeller blade during one period, $-\beta$

$f_{x,i,s}$ of the propeller blade are presented.

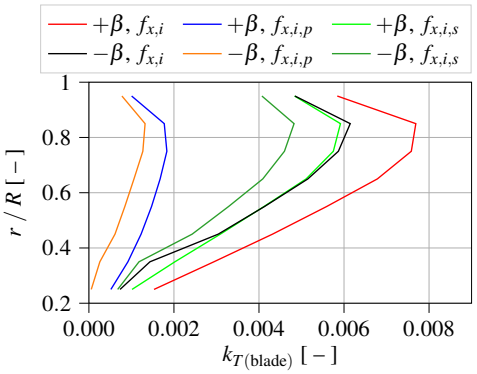

Figure 56: Radial distribution of the average axial force for propeller blade sections

Propeller inflow analysis

Nominal wake

For a better understanding of the hydrodynamic behavior of the propeller, the nominal wake at the propeller plane is shown in Figures 57, 58, 59 and 60 for straight ahead and static drift conditions. The nominal velocity distribution in the propeller plane is evaluated for positive and negative drift angles. Figure 57 shows the axial u_x and tangential u_t velocity components at straight ahead. The radial positions of the blade segments are outlined as black lined circles. The axial velocity component shows a symmetrical distribution, while the tangential one shows an anti-symmetrical distribution as expected.

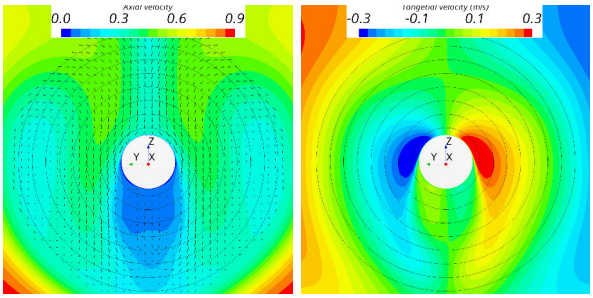

(a) u_x **(b)** u_t

Figure 57: Axial (u_x) and tangential velocity (u_t) component in the propeller plane, straight, RANS k-ω-SST

At static drift a high gradient of the axial velocity occurs and the slow stream region in the lee side is enlarged as shown in Figure 58 and Figure 59 for the positive and negative drift cases respectively. Consequently, the rotation direction of the ABV vortex has a strong influence on the tangential velocity. As shown in Figure 60, the rotation direction has an inflating effect on the

thrust forces in the positive drift case, since two larger areas of negative tangential velocity appear, in which the relative tangential velocity between the flow and the propeller is increased. Figure 60 shows the areas of increased and decreased tangential velocity in the propeller plane for both drift cases.

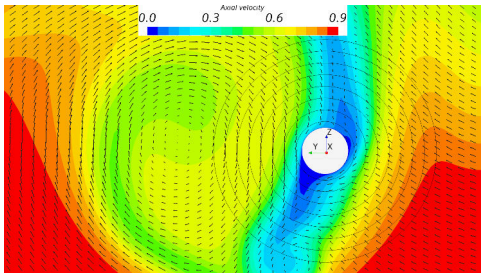

Figure 58: Axial (u_x) velocity component in the propeller plane, $+\beta$, RANS k-ω-SST

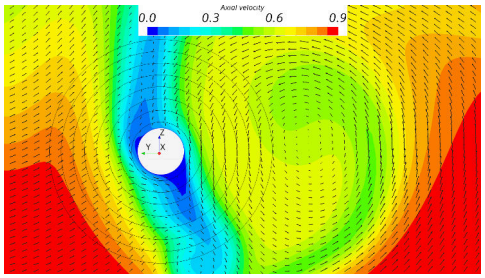

Figure 59: Axial (u_x) velocity component in the propeller plane, $-\beta$, RANS k-ω-SST

Figure 61 shows the distribution of the axial velocity component for radial sections at positive drift. There are two widely spread plateaus around 90° and 270°. The curves are symmetric for positive and negative drift.

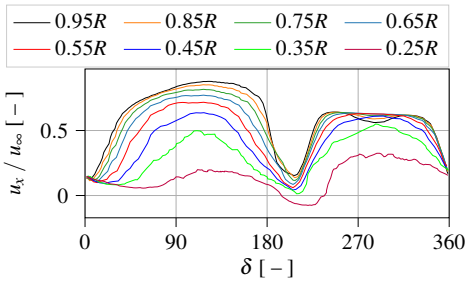

Figure 61: Axial velocity component over one propeller revolution in the propeller plane, $+\beta$

The distribution of u_t for positive and negative drift cases is shown in Figure 62 and Figure 63 respectively. While u_t is mostly negative for positive drift, an opposite trend is observed for negative drift. This explains the deviations

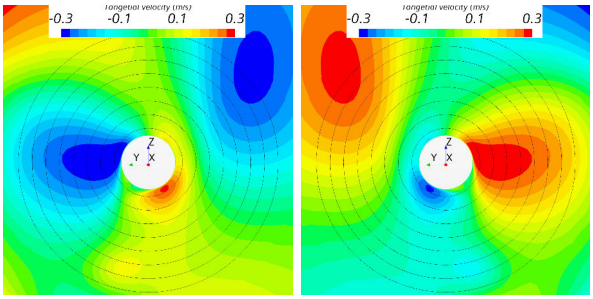

(a) $+\beta$ **(b)** $-\beta$

Figure 60: Tangential velocity (u_t) component in the propeller plane, RANS k-ω-SST

in the propeller thrust observed between positive and negative drift in the previous section.

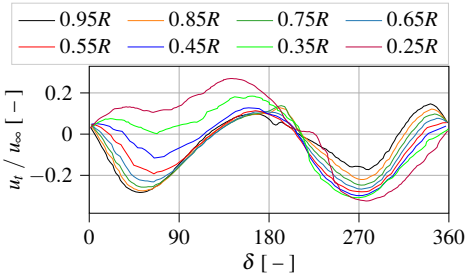

Figure 62: Tangential velocity component over one propeller revolution at propeller plane, $+\beta$

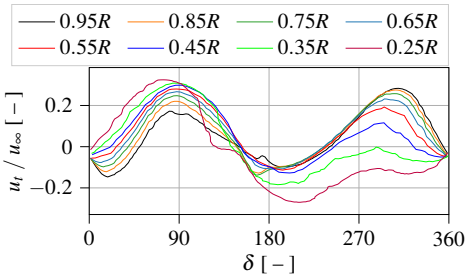

Figure 63: Tangential velocity component over one propeller revolution at propeller plane, $-\beta$

This effect leads to a locally increased angle of attack α at a positive drift. The local angle of attack is estimated based on the nominal wake according to:

$$\alpha = \arctan\left(\frac{u_x}{\omega r - u_t}\right) - \phi \,, \tag{1}$$

where ϕ is the propeller blade pitch, which changes in radial direction. The angle of attack is illustrated for straight ahead (Fig. 64a) , positive drift (Fig. 64b) and static drift (Fig. 64c).

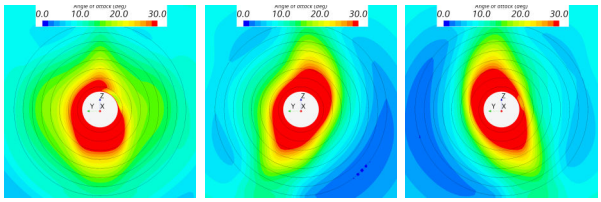

(a) straight **(b)** $+\beta$ **(c)** $-\beta$

Figure 64: Angle of attack α in the propeller plane, different conditions, RANS k-ω-SST

Figure 65 shows the axial and tangential velocities as well as the angle of attack obtained by the IDDES simulation for the negative drift case. Due to the influence of ABV, the tangential velocities at each radius are reduced and this effect leads to particularly smaller angles of attack in the outer radius.

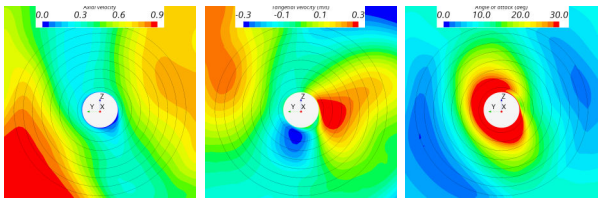

(a) u_x **(b)** u_t **(c)** α

Figure 65: Axial (u_x), tangential (u_t) velocity component and angle of attack in the propeller plane, $-\beta$, IDDES k-ω-SST

Figure 66 illustrates the difference in the angle of attack between the straight-ahead and static drift cases. It clearly shows how the angle of attack is reduced at 3 and 9 o'clock positions. These minima are more pronounced in the case of a negative drift.

Compared to the straight-ahead condition, a clear increase of over 60% in the nominal velocity on the lee side can be observed as shown in Figure 67.

The radial variation of the angle of attack over one revolution is shown in Figure 68 and the Figure 69 for positive and negative drift angle, respectively. The results correspond directly to the radial distribution of the axial thrust force and persistently underlines the findings obtained so far, see Figure 56. At this point, it should be noted that the radial sections greater than $0.4R$ have the main contribution to the thrust and the induced velocity components of the propeller blades were not considered in the present analysis.

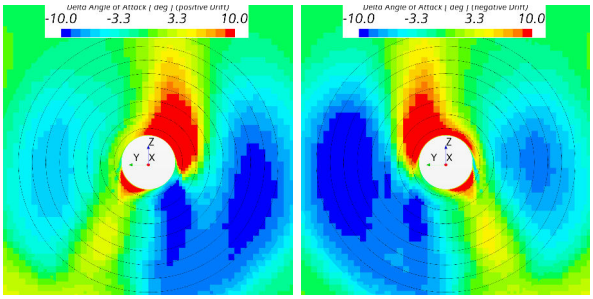

(a) $+\beta$ **(b)** $-\beta$

Figure 66: Difference in angle of attack α between drift and straight-ahead condition, RANS k-ω-SST ($\alpha_{\text{drift}} - \alpha_{\text{straight}}$)

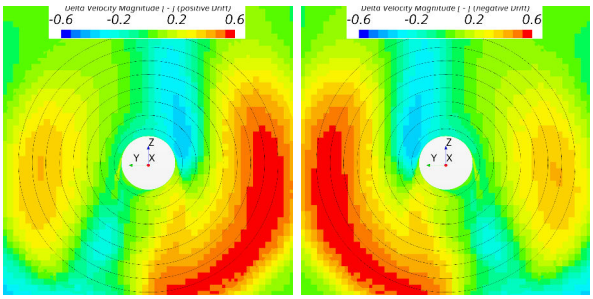

(a) $+\beta$ **(b)** $-\beta$

Figure 67: Difference in velocity magnitude $|u|$ between drift and straight-ahead condition, RANS k-ω-SST, ($|u|_{\text{drift}} - |u|_{\text{straight}}$)

Influence of the induced velocity components

The previously presented results are obtained from simulations of the JBC hull without propeller. The calculated velocity distribution using RANS simulation under consideration of the influence of the working propeller for positive and negative drift angles can be seen in Figure 70 and Figure 71. The figures show the distribution of axial and total velocity components at a distance of 20% of the propeller radius R upstream of the propeller. The total velocity is the resulting velocity from axial and tangential velocity components. Also included in the figures is the resulting angle of attack.

The results show the extent to which the induced velocities influence the local angle of attack. The angle of attack increases inside the slow stream region and decreases outside of it for both drift cases. However, the reduction in the negative drift angle case is much stronger than the positive one.

CONCLUSION AND OUTLOOK

The hull-propeller-interaction for the static drift condition at a constant rotation rate of the propeller is investigated

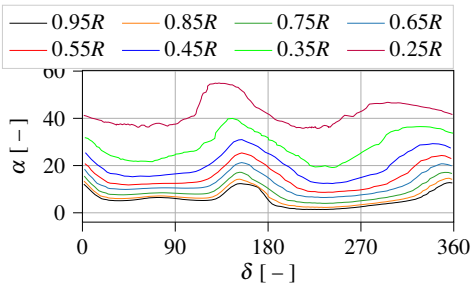

Figure 68: Angle of attack over one propeller revolution at propeller plane, $+\beta$

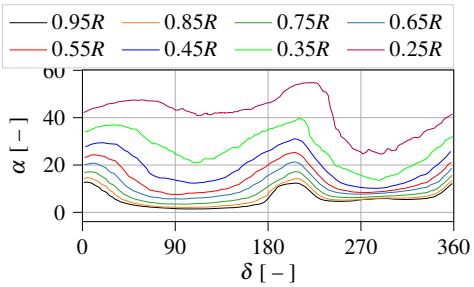

Figure 69: Angle of attack over one propeller revolution at propeller plane, $-\beta$

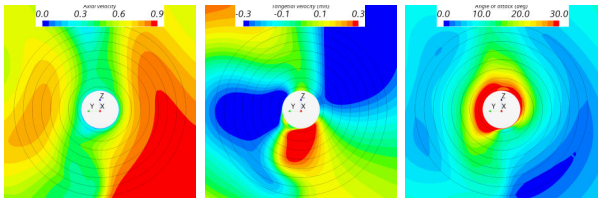

(a) u_x **(b)** u_t **(c)** α

Figure 70: Axial velocity component, total velocity and angle of attack with induced velocity component, $+\beta$, RANS k-ω-SST

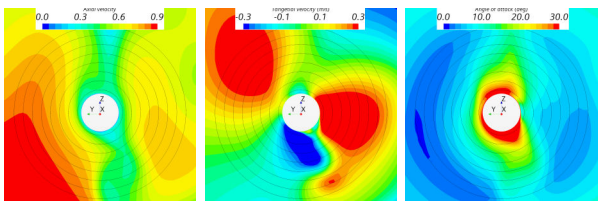

(a) u_x **(b)** u_t **(c)** α

Figure 71: Axial velocity component, total velocity and angle of attack with induced velocity component, $-\beta$, RANS k-ω-SST

and detailed insights into the flow characteristics are given. Initially, the properties of the fore-body vortex were studied intensively by comparing the results of RANS, DDES and IDDES simulations as well as experimental data. Principally, a good agreement between different cases has been attained. Despite a consistent velocity in the vortex core by all methods, an underestimated vorticity is observed due to a significantly stronger widening of the vortex in RANS. However, the results DDES and IDDES show consistency with the level of the measured vorticity and TKE in the experimental investigation.

Based on the simulation conducted based on RANS-k-ω-SST as well as DDES/IDDES-k-ω-SST simulations, the presented results indicate that an interaction of the hull's vortex structure with the propeller flow is indeed important, despite the lower than expected dependency of the results on the turbulence modeling. Nevertheless, a reliable prediction for the velocity field is obtained with all used methods. Only the hybrid approaches were able to efficiently capture TKE. This allows for an accurate prediction of the thrust fluctuations . The computational effort per time step increases by 5% for DDES and about 15% for IDDES compared to the RANS method.

Furthermore, the comparison of the experimental results with those of the numerical simulations in the after-body region shows that the numerical simulations provide a reliable prediction. In addition, the measured propeller thrust could be reproduced. An extensive study of propeller blade forces has shown details of the mechanisms causing strong differences for positive and negative drift. The detaching aft-body vortex is equidirectional with the propeller at positive drift and contra-rotating at negative drift. This effect leads to a drastic change of propeller thrust forces. A further analysis of the influence of the drift condition on the local inflow angles of the propeller blades has been conducted. Results obtained by RANS simulation have shown good agreement of the velocity components with measured flow fields within the aft-body vortex, which makes it reliably applicable in investigations of propulsion problems. On the other hand, vortex-resolving approaches showed a better agreement with measurements of the fore-body side vortex. On fine grids there were only few deviations between the approaches applied.

In the future, simulations of further operating conditions of the propeller will be considered. Also, calculations for a pure sway motion will be performed.

Understanding the hydrodynamic propeller performance in inclined flow is especially important for maneuvering conditions of ships. The inclusion of the rudder in the study will enhance the value of the results for practical

applications. A reliable prediction of the hull-propeller interaction parameters is important for the further investigation of the efficiency of, for example, energy saving devices.

ACKNOWLEDGEMENTS

This work was funded by the German Federal Ministry for Economic Affairs and Climate Action under the aegis of the BMWK-project *PSDMan* within the framework program "Maritime Forschungsstrategie 2025". The authors express their gratitude to the industrial cooperation partners in the research project: Becker Marine Systems GmbH (www.becker-marine-systems.com), IBMV Maritime Innovationsgesellschaft mbH (www.ibmv.de) and Schiffbau Versuchsanstalt Potsdam GmbH (www.sva-potsdam.de) for their valuable support.

REFERENCES

T. Hino, F. Stern, L. Larsson, M. Visonneau, N. Hirata and J. Kim, "Numerical Ship Hydrodynamics - An Assessment of the Tokyo 2015 Workshop", Springer, 2021.

M. Visonneau, G.B. Deng, E. Guilmineau, P. Queutey and J. Wackers, "Local and Global Assessment of the Flow around the Japan Bulk Carrier with and without Energy Saving Devices at Model and Full Scale", Proceedings of the 31th Symposium on Naval Hydrodynamics, 2016, pp. 1–20.

F. Ismail, P.M. Carrica, T. Xing and F. Stern, "Evaluation of linear and nonlinear convection schemes on multidimensional non-orthogonal grids with applications to KVLCC2 tanker", International Journal for Numerical Methods in Fluids, 2009.

T. Xing, S. Bhushan and F. Stern, "Vortical and turbulent structures for KVLCC2 at drift angle 0, 12, and 30 degrees", Ocean Engineering, Vol. 55, 2012, pp. 23–43.

C. Fureby, S. Toxopeus, M. Johansson, M. Tormalm and K. Petterson, "A computational study of the flow around the KVLCC2 model hull at straight ahead conditions and at drift", Ocean Engineering, Vol. 118, 2016, pp. 1–16.

D.F. Feder, I. Shevchuk, A. Sahab, L. Gerwers and M. Abdel-Maksoud, "Fore-Body Side Vortex of KVLCC2 at 30 Degree Drift: A Trailing Vortex Resolved with DES and Compared to PIV Data", Open Journal of Fluid Dynamics, Vol. 09, No. 04, 2019, pp. 303–325.

I. Shevchuk, A. Sahab and M. Abdel-Maksoud, "Experimental and numerical studies of the flow around the JBC hull form at straight ahead condition and 8° drift angle", 33rd Symposium on Naval Hydrodynamics, Osaka, Japan, 2020.

N. Abbas, N. Kornev, I. Shevchuk and P. Anschau, "CFD prediction of unsteady forces on marine propellers caused by the wake uniformity and nonstationarity", Ocean Engeneering, Vol. 104, pp. 659-672, 2015.

M. Visonneau, E. Guilmineau and G. Rubino , "Computational Analysis of the Flow around a Surface Combatant at 10° Static Drift", 7th Symposium on Hybrid RANS-LES Methods, September 2018, Berlin, Germany.

Y. Levy, D. Degani, and A. Seginer , "Graphical Visualization of Vortical Flows by Means of Helicity", AIAA J., 28(8):1347–1352, August 1990.

S. Sahab, P. Sumislawski, and M. Abdel-Maksoud, "Experimental investigation on the wake of the Japan Bulk Carrier model with Stereoscopic and Tomographic Particle Image Velocimetry", 34th Symposium on Naval Hydrodynamics, Washington, United States, 2022.

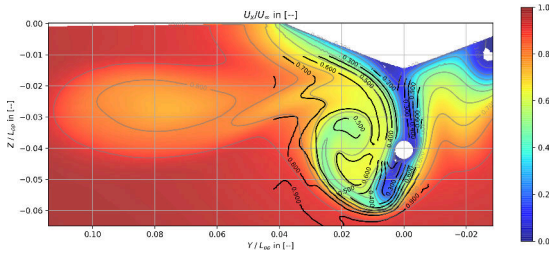

(a) RANS k-ω-SST, u_x

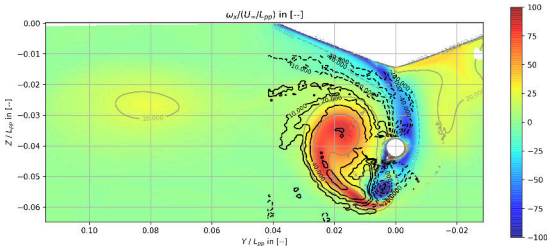

(b) RANS k-ω-SST, ω_x

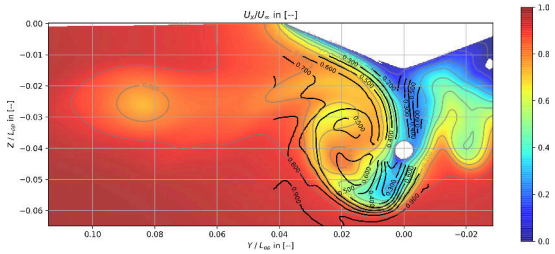

(c) IDDES k-ω-SST, u_x

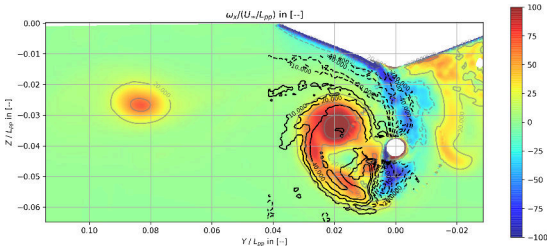

(d) IDDES k-ω-SST, ω_x

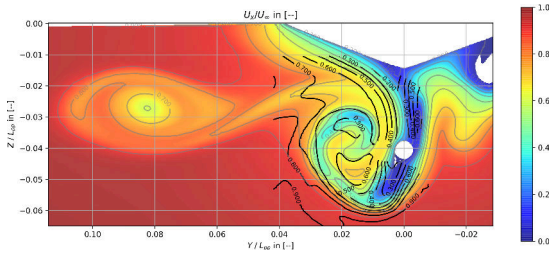

(e) DDES k-ω-SST, u_x

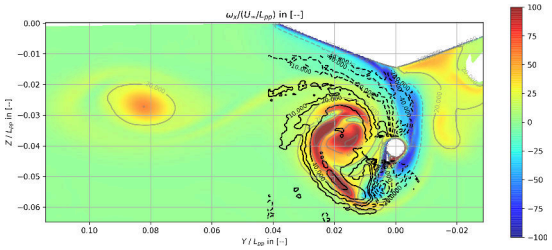

(f) DDES k-ω-SST, ω_x

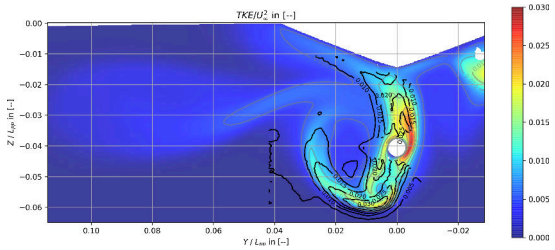

(g) RANS k-ω-SST, k

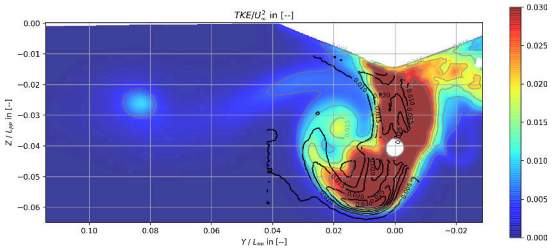

(h) IDDES k-ω-SST, k

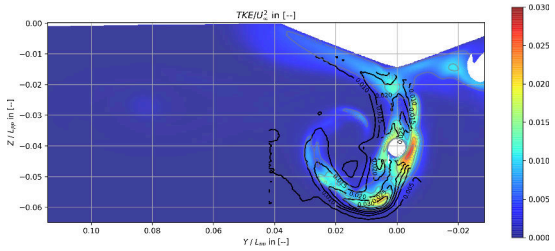

(i) DDES k-ω-SST, k

Figure 72: Comparison of CFD and EFD results, measurement plane S4, propeller plane, $+\beta$

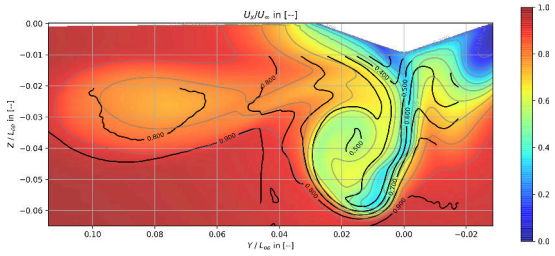

(a) RANS k-ω-SST, u_x

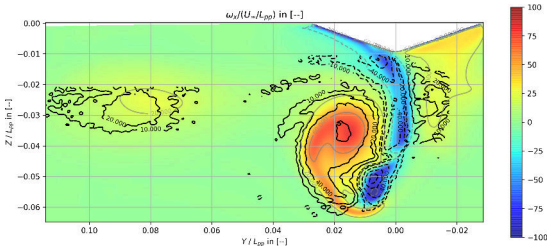

(b) RANS k-ω-SST, ω_x

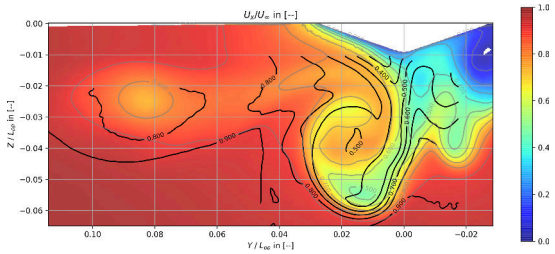

(c) IDDES k-ω-SST, u_x

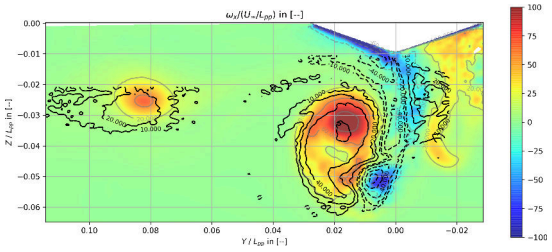

(d) IDDES k-ω-SST, ω_x

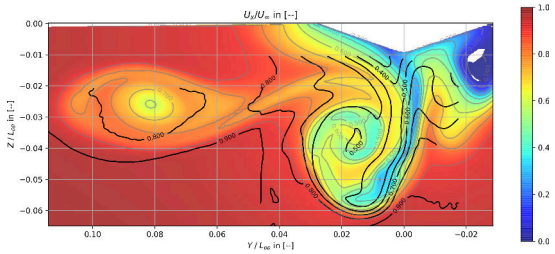

(e) DDES k-ω-SST, u_x

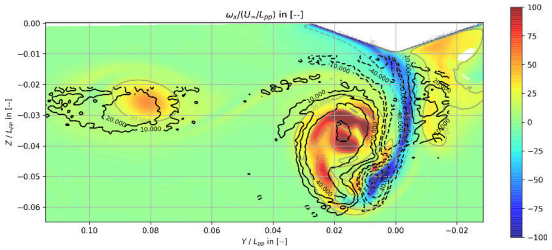

(f) DDES k-ω-SST, ω_x

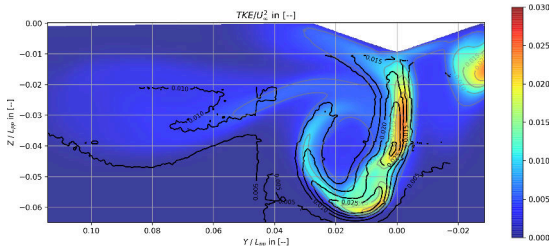

(g) RANS k-ω-SST, k

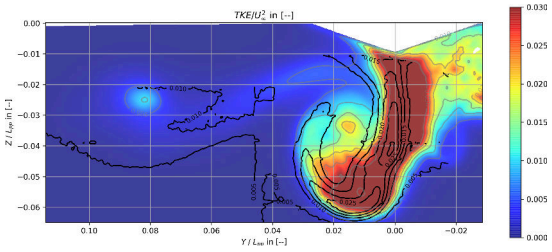

(h) IDDES k-ω-SST, k

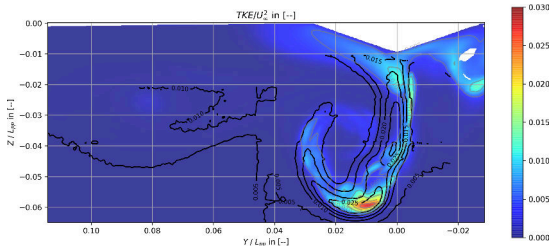

(i) DDES k-ω-SST, k

Figure 73: Comparison of CFD and EFD results, measurement plane S7, aft perpendicular, $+\beta$

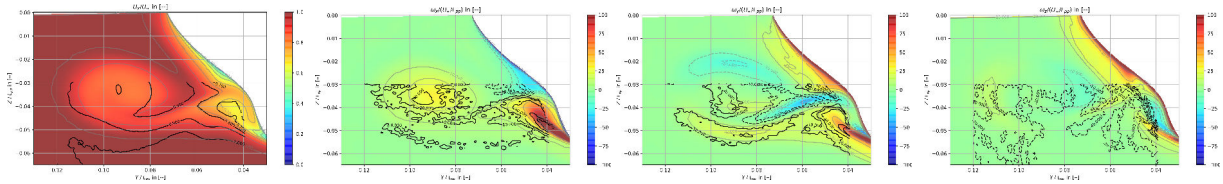

(a) RANS k-ω-SST, u_x **(b)** RANS k-ω-SST, ω_x **(c)** RANS k-ω-SST, ω_y **(d)** RANS k-ω-SST, ω_z

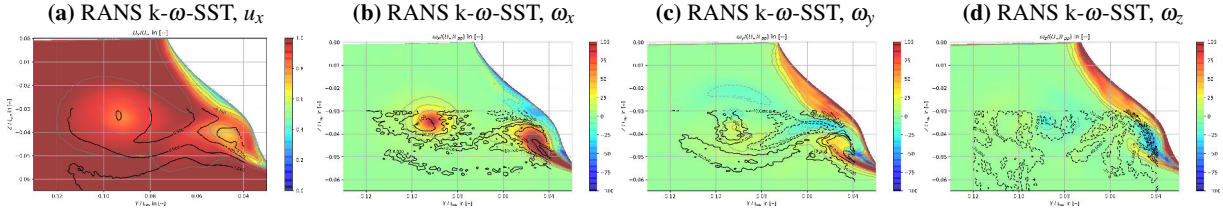

(e) IDDES k-ω-SST, u_x **(f)** IDDES k-ω-SST, ω_x **(g)** IDDES k-ω-SST, ω_y **(h)** IDDES k-ω-SST, ω_z

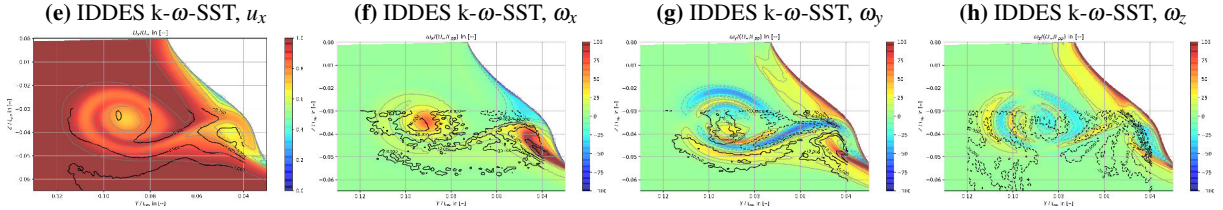

(i) DDES k-ω-SST, u_x **(j)** DDES k-ω-SST, ω_x **(k)** DDES k-ω-SST, ω_y **(l)** DDES k-ω-SST, ω_z

Figure 74: Comparison of CFD and EFD results, FSV, $0.1L_{pp}$, $+\beta$

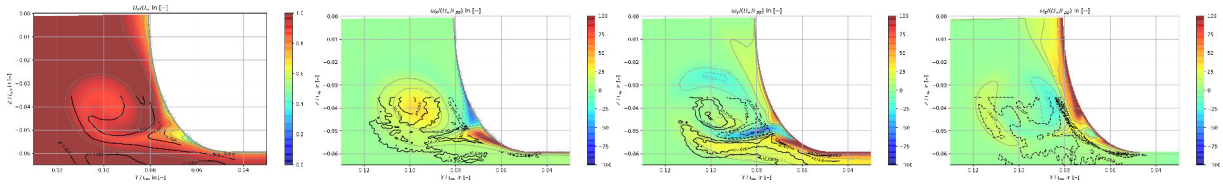

(a) RANS k-ω-SST, u_x **(b)** RANS k-ω-SST, ω_x **(c)** RANS k-ω-SST, ω_y **(d)** RANS k-ω-SST, ω_z

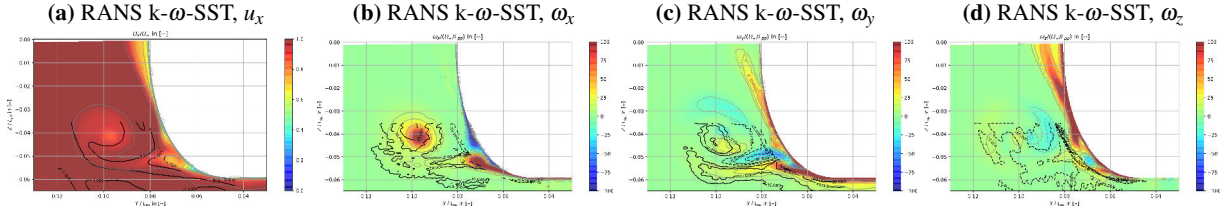

(e) IDDES k-ω-SST, u_x **(f)** IDDES k-ω-SST, ω_x **(g)** IDDES k-ω-SST, ω_y **(h)** IDDES k-ω-SST, ω_z

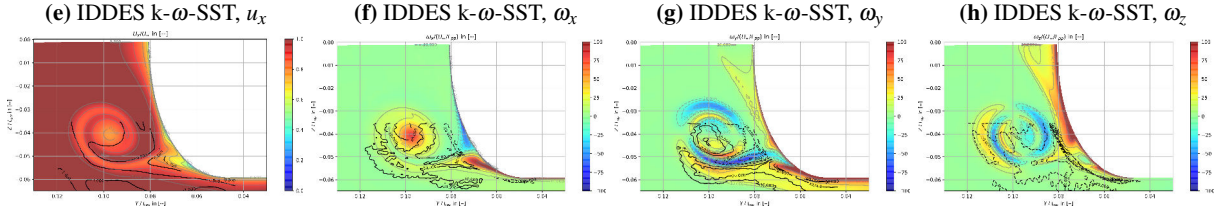

(i) DDES k-ω-SST, u_x **(j)** DDES k-ω-SST, ω_x **(k)** DDES k-ω-SST, ω_y **(l)** DDES k-ω-SST, ω_z

Figure 75: Comparison of CFD and EFD results, FSV, $0.2L_{pp}$, $+\beta$

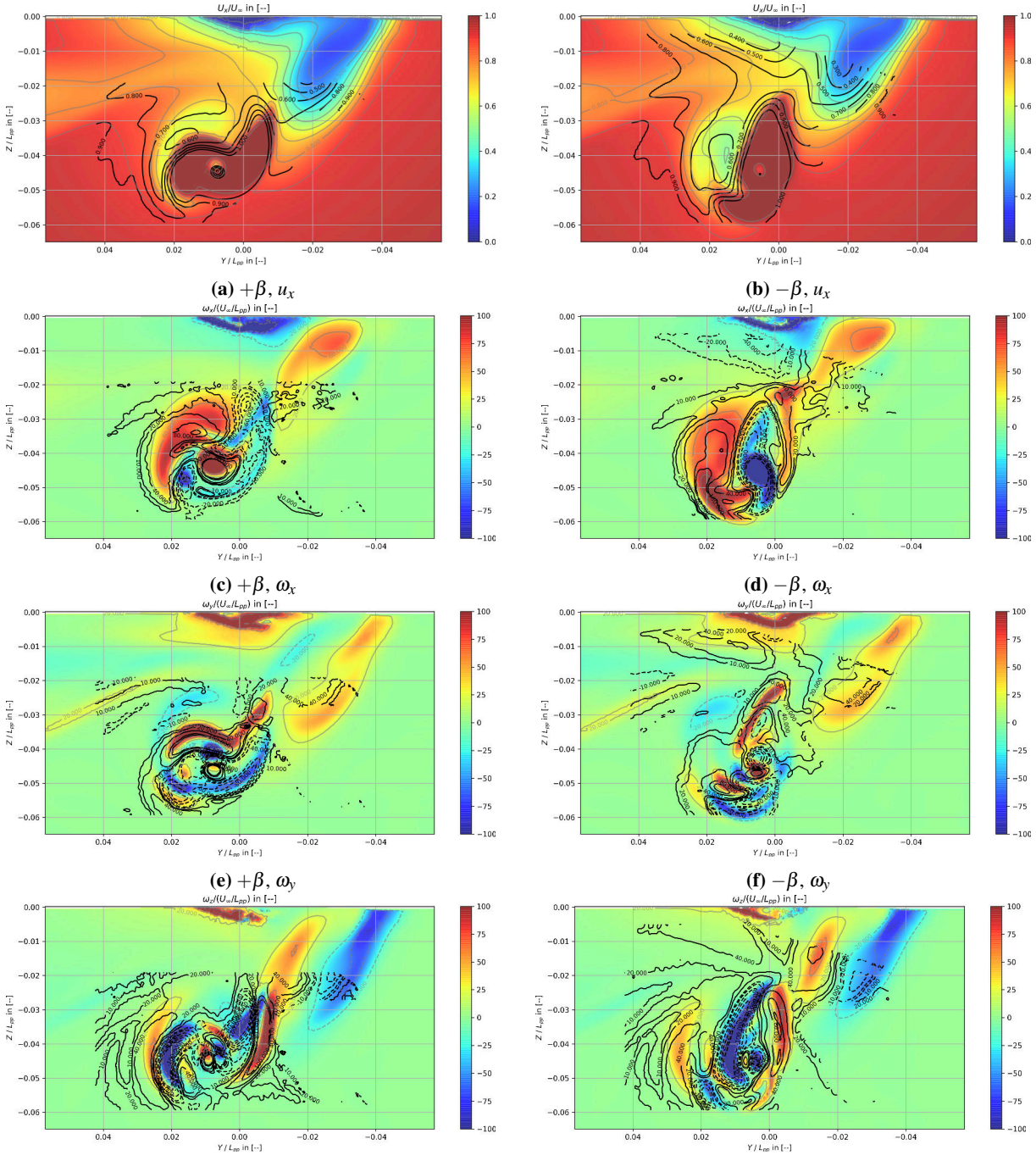

(a) $+\beta$, u_x **(b)** $-\beta$, u_x

(c) $+\beta$, ω_x **(d)** $-\beta$, ω_x

(e) $+\beta$, ω_y **(f)** $-\beta$, ω_y

(g) $+\beta$, ω_z **(h)** , $-\beta$, ω_z

Figure 76: CFD vs EFD, velocity and vorticity components, positive and negative drift, RANS k-ω-SST, measurement plane S7', transom stern

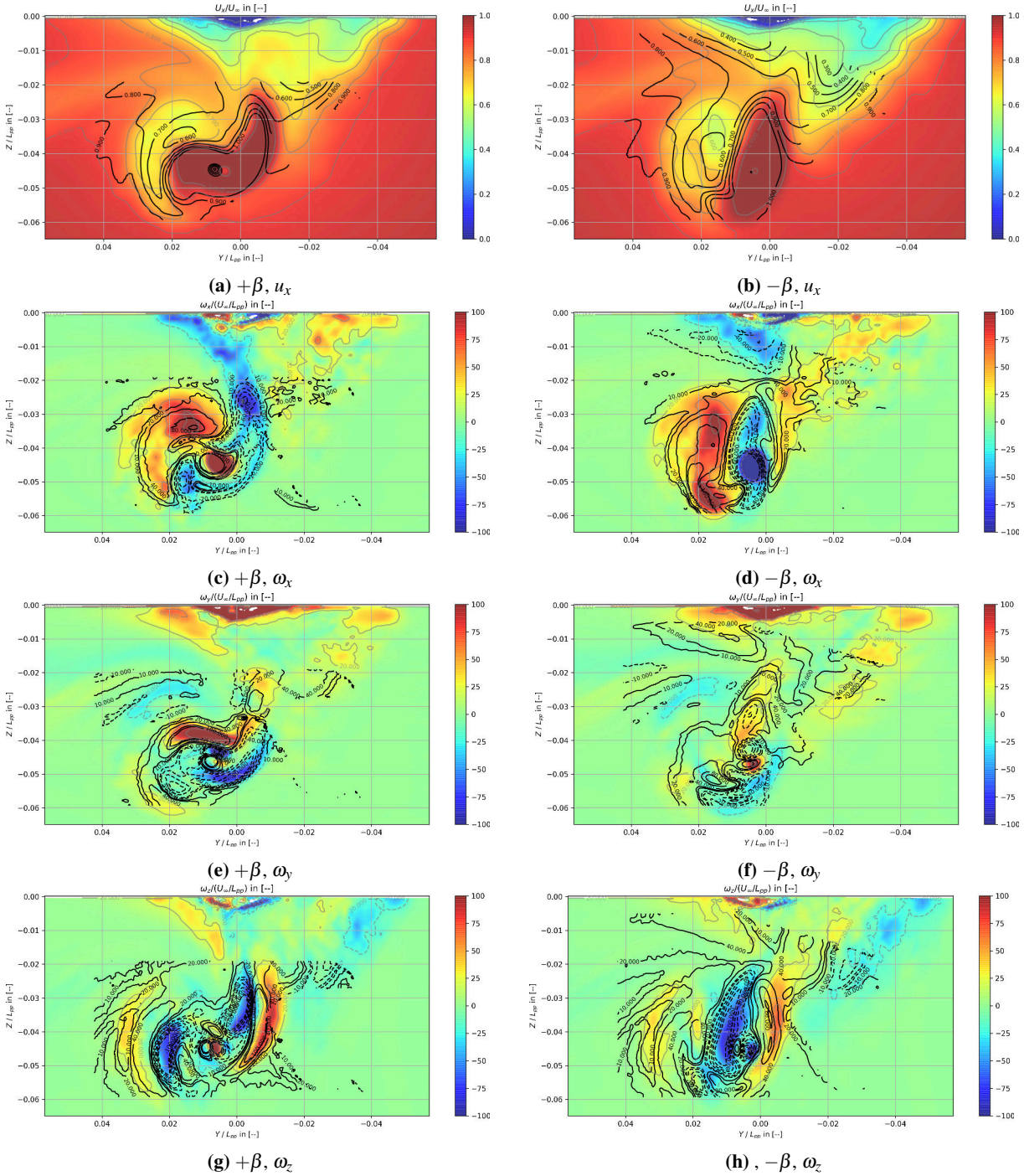

(a) $+\beta$, u_x **(b)** $-\beta$, u_x

(c) $+\beta$, ω_x **(d)** $-\beta$, ω_x

(e) $+\beta$, ω_y **(f)** $-\beta$, ω_y

(g) $+\beta$, ω_z **(h)** , $-\beta$, ω_z

Figure 77: CFD vs EFD, velocity and vorticity components, positive and negative drift, IDDES k-ω-SST, measurement plane S7', transom stern

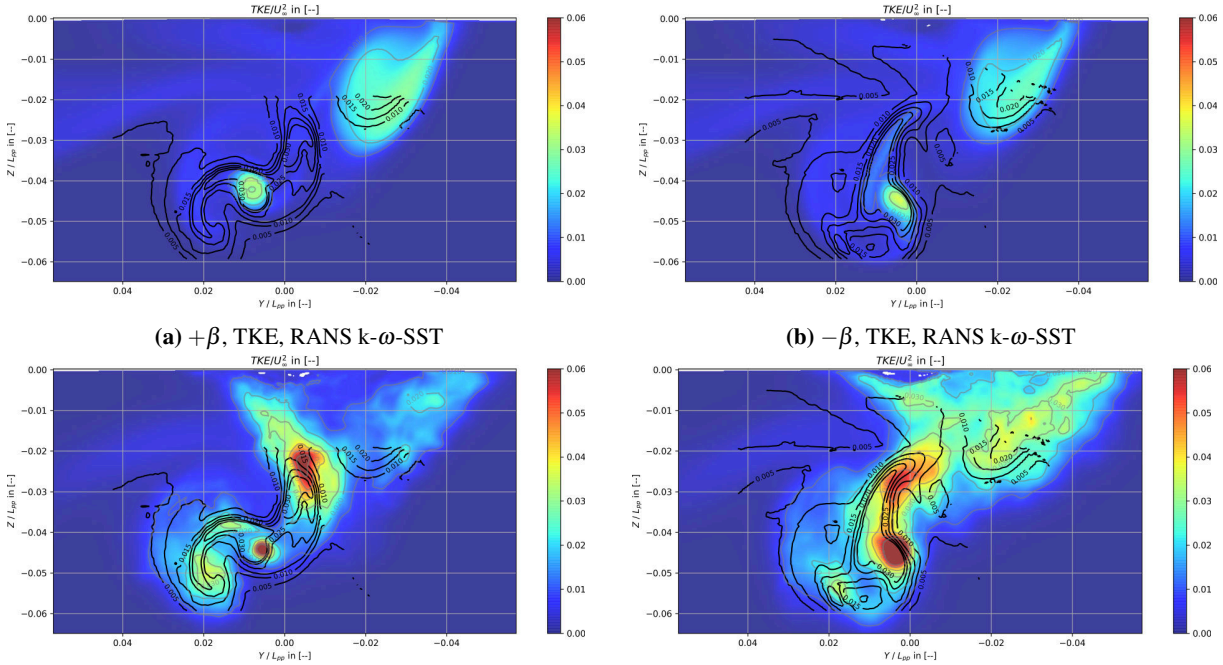

(a) $+\beta$, TKE, RANS k-ω-SST

(b) $-\beta$, TKE, RANS k-ω-SST

(c) $+\beta$, TKE, IDDES k-ω-SST

(d) $-\beta$, TKE, IDDES k-ω-SST

Figure 78: CFD vs EFD, TKE, positive and negative drift, RANS and IDDES k-ω-SST, measurement plane S7', transom stern

DISCUSSION

Comment 1: For the reader, however, additional information about unsteady thrust and torque of the entire propeller would be of great interest.
Reply 1: In Figures 64a and b the 1/5th of the total thrust is shown for the cases with positive and negative drift respectively, whereas in Figures 64c and d the 1/5th of the torque can be seen for the same cases. The following conclusions can be drawn from these plots. First, the periodic oscillations of the propeller forces are much more intense under the pure drift condition as compared to straight ahead. Second, the positive drift angle yields higher K_T and K_Q values. Third, on top of the periodic fluctuations the application of the IDDES introduces also a significant unsteadiness to the thrust and torque signal, following from the large-scale dynamics of the wake.

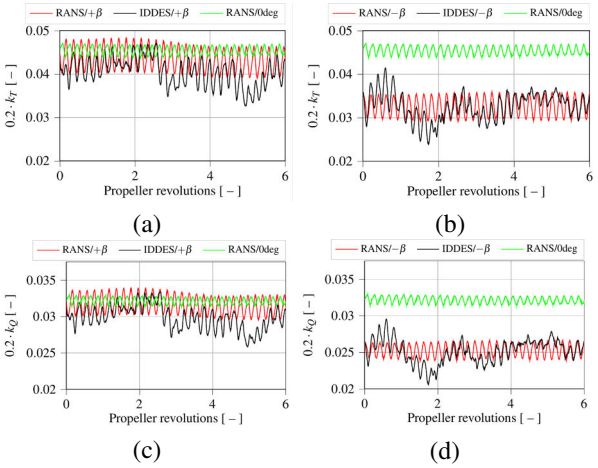

Figure 79: Time evolution of thrust and torque coefficients for different conditions: a,c - positive drift angle, b,d - negative drift angle

Comment 2: In selecting their computational domain how much do they consider the flow field would have been influenced by the use of a domain that was not identical to the constrained walls of the wind tunnel used in the experiments?
Reply 2: In order to answer this question we conducted two computations with the configurations, different from the one considered in this work: in the first one the "infinite" computational domain was used (c2) and in the second, the wall boundary condition (no-slip) was applied at side walls and top/bottom (c3). The results of these two cases were compared with the original configuration described in the paper (c1). In Figures 65a-f one can see the comparison of the mentioned configurations for the longitudinal velocity field and the TKE distribution in the propeller plane. Obviously, no significant changes changes can be seen. The minor variations of the solution can be attributed to the statistical convergence of the mean and the moment of the velocity field.

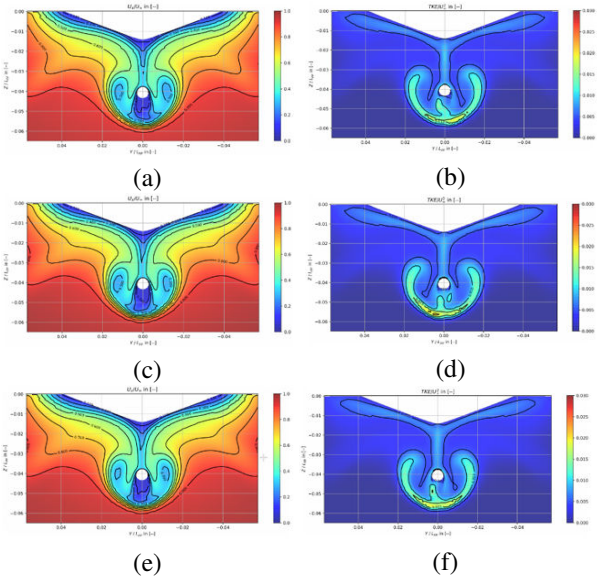

Figure 80: Distribution of the longitudinal velocity (left column) and the TKE (right column) for three computational domain configurations: a,b - C1, c,d - C2, e,f - C3

Comment 3: Could they comment on the difference in thrust loading condition between their selected rpm and hence thrust/torque performance of the propeller with that expected at the full scale operating condition?
Reply 3: C_{th} in this study is approximately 0.5. C_{th} of the full scale ship is unknown and cannot be estimated from available computational/experimental results.

Comment 4: Reason for the differences in forces between coarse and fine grids?
Reply 4: In Figures 66 and 67 the distribution of the shear stress at the hull and the resistance coefficent distribution of the ship length is shown. It can be seen that on the coarse grid the wall shear stress is much higher that on the fine one at the bilge in the stern region. Consequently, a stronger separation is observed, which leads to the difference in the pressure component of the resistance.

Comment 5: Could the authors provide some more details about the computational expenses of the different methods?
Reply 5: Benchmarks have shown, that the computational effort increases by around 5% for DDES and 15% for IDDES as compared to RANS. Calculations were performed using the finest grid (32M) on a 32-core node. For details see the Figure 68

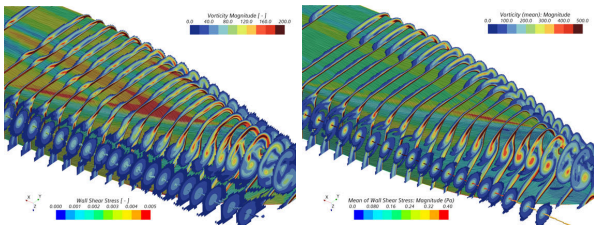

(a) (b)

Figure 81: Wall shear stress distribution on the ship hull for the coarse (a) and fine (b) grids

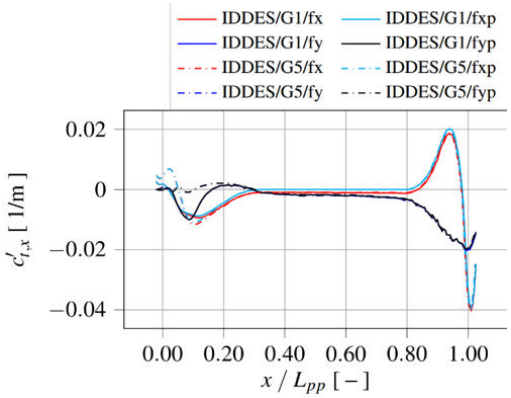

Figure 82: Resistance coefficient distribution over the ship length

Comment 6: Higher values of the TKE with IDDES are surprisingly very different from what is predicted by DDES, why? Is the shielding function so influential.
Reply 6: Our assumption is that before separation, the total Reynolds stresses near the wall are not sufficient in IDDES to provide the same wall-normal momentum transport as in RANS and as a result the flow separates earlier and oscillates more intensively in the recirculation region (as it would have oscillated if the Reynolds stresses were resolved better), which also yields much higher TKE values. The first solution is the use of the shielding function as in DDES and the second one is the increase of the resolved Reynolds stresses in the grey area by the introduction of the artificial turbulent fluctuations. Unfortunately, the performance of DDES shielding also deteriorates on finer grids.

Method	$Co_{\max}$ [−]	Co_{mean} [−]	Solver Time per Iteration [s]	Solver CPU Time per Time Step [s]
RANS	1.005	0.0135	11.52	1405
DDES	0.651	0.0133	11.97	1475
IDDES	1.696	0.0136	13.50	1638

Figure 83: Comparison of the computational time for different methods on the fine grid

Comment 7: Please, also provide the local cell size in the core of the FSV and ABV vortex in terms of Taylor scale.
Reply 7: The cell size ratio is 2:1 (CFD:EFD, 2mm to 1mm on the finest computational grid), whereas the Taylor microscale is estimated to be approximately $\lambda_g = 0.3$mm for both vortices. Which yields $\lambda_g/\Delta \approx 0.15$.

Comment 8: Could they comment also on the likely tip Mach No and what influence Reynolds number would play on the flow compared to the full scale ship.
Reply 8: The local tip Mach No is 0.13. An influence of the Mach No is assumed to be negligible.

Comment 9: Could the authors briefly comment on the uncertainties when measuring the hydrodynamic forces acting on hull and propeller?
Reply 9: Uncertainty of the measured hydrodynamic forces is less than 0.15%.

Comment 10: Could the authors explain how the define and calculate the wake fraction under drift angle?
Reply 10: The wake is determined for the axial velocity component in the same manner as at the straight ahead condition: $w = 1 - \frac{\overline{u}_x}{u_\infty}$.

Comment 11: If the authors briefly addressed relevant scaling effects in a qualitative manner, it would be of great value for the reader
Reply 11: The full scale JBC has not been investigated so far.